

A FUNCTIONAL-DATA APPROACH TO THE ARGO DATA

BY DREW YARGER[†], STILIAN STOEV^{*}, AND TAILEN HSING^{*}

University of Michigan

The Argo data is a modern oceanography dataset that provides unprecedented global coverage of temperature and salinity measurements in the upper 2,000 meters of depth of the ocean. We study the Argo data from the perspective of functional data analysis (FDA). We develop spatio-temporal *functional kriging* methodology for mean and covariance estimation to predict temperature and salinity at a fixed location as a smooth function of depth. By combining tools from FDA and spatial statistics, including smoothing splines, local regression, and multivariate spatial modeling and prediction, our approach provides advantages over current methodology that consider pointwise estimation at fixed depths. Our approach naturally leverages the irregularly-sampled data in space, time, and depth to fit a space-time functional model for temperature and salinity. This model is then used to provide predictions continuously as a function of pressure. The resulting methodology provides new tools for scientific problems where the dependence on depth must be considered. We conclude with two important examples on the estimation of the ocean heat content and the mixed layer depth.

1. Introduction. The development of technology has vastly increased the amount and complexity of data available that monitor the Earth’s environment. We focus on one type of such data collected by the Argo project, an international collaboration that oversees more than 3,800 devices called floats which measure the temperature and salinity of the oceans. Each float periodically ascends from 2 kilometers deep while collecting temperature and salinity measurements as a function of pressure—a proxy for depth, with 1 decibar (dbar) roughly corresponding to 1 meter of depth. These data, referred to as profiles, are transmitted over satellite to data processing centers along with the float’s coordinates and time stamps. The drifting floats collect approximately 100,000 profiles each year, resulting in a large and complex space-time dataset, indexed by longitude, latitude, time, and pressure. The global coverage of the data and the depth of measurements provide previously unavailable richness of oceanography data (see Figure 1). The Argo data has begun to play a critical part in measuring sea level rise, currents, and the global distribution of temperature and salinity of the oceans (see [Argo \(2000\)](#) for more information). The oceans play a major role in the Earth’s climate; for example, [Roemmich et al. \(2015\)](#) uses Argo data to study the warming oceans, which account for more than 90% of the net planetary energy increase. More than 1,500 papers that use Argo data have been published in the past five years; however, the Argo data has just begun to see research in the statistics community. To our

^{*}Supported by the NSF Grant DMS-1916226

[†]Supported by the NSF Grants DMS-1646108 and DGE-1841052

Keywords and phrases: functional data analysis, Matérn, oceanography, spatial statistics, splines

knowledge, [Kuusela and Stein \(2018\)](#) is the first such publication, which enumerates some directions for future statistical research for the Argo data.

We address the statistical problem of functional kriging, i.e., mapping or spatio-temporal prediction, of temperature and salinity viewed as functions of pressure. In the context of the Argo data, each profile can be considered functional data, with measurements observed as a function of pressure for a fixed time and location. In this framework, we use nearby profiles in space and time to estimate temperature and salinity between the profile locations. This is done by using functional models for the mean and space-time covariance structure, which also yields uncertainties and confidence sets for the functional kriging estimates. The FDA approach provides computational, scientific, and methodological advantages over current approaches that consider models for one pressure level at a time by linearly interpolating temperature and salinity onto that pressure (e.g. [Roemmich and Gilson, 2009](#); [Kuusela and Stein, 2018](#)). First, the FDA approach provides a principled way to fully leverage the irregularly-sampled measurements in pressure. Sharing information across pressure enables us to use measurements without perturbation and fully describe the dimension of pressure. Second, the estimated functions capture the complex structure in the oceans as a function of pressure that arises from the oceans' stratification and mixing. In addition, the FDA approach naturally yields estimates of derivatives and integrals over the entire pressure dimension which can provide new insight into key scientific problems.

We directly compare our FDA approach with current ones that first linearly interpolate each profile onto fixed pressure levels. While such an interpolation simplifies the data for the subsequent modeling compared to irregularly sampled pressures, it also introduces error or neglects data depending on whether the profiles observed are *sparse* or *dense* in pressure. Since Argo profiles typically range in number of observations from around 60 to 1,000 measurements, the Argo data present a combination of such heterogeneous data. When sparse functional data are observed, that is, there are just a few measurements per profile, interpolating or presmoothing each curve can decrease accuracy in comparison to pooling data from profiles ([Hall, Müller and Wang, 2006](#)). When dense functional data is available, only some observations are used to interpolate onto pressure levels, and the smaller features of the temperature and salinity in the pressure dimension will be undetected. The FDA approach both avoids the interpolation error for the sparsely-observed profiles and leverages all measurements from each profile, and thus it describes the pressure dimension in more intricate detail. Furthermore, when predicting at a large number of pressure levels (e.g. the 58 [Roemmich and Gilson, 2009](#), pressure levels or more), the functional approach can considerably reduce computations by sharing information across pressure and providing a functional prediction. Perhaps most notably, estimating at fixed levels limits one's ability to predict derivative and integral functionals of the temperature and salinity, since these must be approximated from discrete predictions. On the other hand, derivatives and integral estimates, along with their uncertainties, are readily available in our functional kriging approach and can be leveraged for scientific problems like ocean heat content and mixed layer depth (see Section 5 below).

In contrast to the classical functional data setting where one observes measurements from independent and identically distributed functions (see e.g. [Ramsay and Silverman, 2013](#)), spatial statistics for functional data has only recently been developed, and most of the literature has focused on the idealized regime where entire functions are observed. For example,

see [Delicado et al. \(2010\)](#), [Kokoszka and Reimherr \(2019\)](#), [Martínez-Hernández and Genton \(2020\)](#), and references therein. Developing methodology and theory for discretely observed spatial functional data has been initially explored in [Zhang and Li \(2020\)](#). The perspective of spatial functional data has mostly been considered in applications to environmental data, for example, in [King et al. \(2018\)](#), [Rodríguez, Dunson and Gelfand \(2009\)](#), [Monestiez and Nerini \(2008\)](#), and [Pauthenet et al. \(2019\)](#). We are not aware of any analysis that uses the spatial FDA approach for data of this size and complexity.

In this paper, we develop new mean and covariance-based methodologies for spatial prediction for functional data in the context of the Argo data. We first introduce our notation for the data and our model:

- **The data:** Denote the data for the i -th profile as $s_i, d_i, y_i, (p_{i,j}, Y_{i,j})_{j=1}^{m_i}$ for $i = 1, \dots, n$ where j indexes the measurement, $s_i = (s_{i1}, s_{i2})$ is its location, $\{d_i, y_i\}$ is its day of year and year, respectively, and $(p_{i,j}, Y_{i,j})_{j=1}^{m_i}$ is the pressure and response measurements. Here, $Y_{i,j}$ denotes temperature or salinity, depending on the context; in actuality, both are observed for each i and j . In this analysis, different floats are treated identically, and the various float characteristics are not used. Data can be viewed using the R Shiny Application referenced in [Appendix A.2](#).
- **The model:** We assume that

$$(1) \quad Y_{i,j} = \mu(s_i, d_i, y_i, p_{i,j}) + X(s_i, d_i, y_i, p_{i,j}) + \epsilon_{i,j}$$

where $\epsilon_{i,j} \sim N(0, \kappa(s, d, p))$ are independent, and for each s, d , and y , $\mu(s, d, y, \cdot)$ is a fixed mean function of pressure, and $X(s, d, y, \cdot)$ for $y = 2007, \dots, 2016$ are realizations from a function-valued random field with mean 0 independent of $\epsilon_{i,j}$. We assume that the distribution of $X(\cdot, \cdot, y, \cdot)$ is the same for all y and that X is weakly dependent in time, so that $X(\cdot, d_i, y_i, \cdot)$ and $X(\cdot, d_j, y_j, \cdot)$ are independent for d_i near d_j and $y_i \neq y_j$.

Our new approach to the estimation of the functional mean μ combines two established approaches in nonparametric statistics: smoothing splines and local polynomial regression. See [Green and Silverman \(1994\)](#) and [Fan and Gijbels \(1996\)](#) for more information on these methodologies, respectively. Specifically, we leverage irregularly sampled data in space and time using local regression to form a spline estimate of the mean function of pressure. This approach can model the strong vertical stratification in the oceans where water masses at different depths can have drastically different characteristics. Our mean estimation reflects the advantages of both of these approaches: computations are reduced by using univariate B-splines, only a subset of the data is used at a time, and nonlinear features of the oceans in pressure, space, and time are naturally estimated. Our extension of [Fan and Gijbels \(1996\)](#) to the case of function-valued data also provides new functional estimates of derivatives of the mean with respect to space and time.

After subtracting the functional mean, we model the covariance structure of the residuals in space, time, and pressure. This consists of three components. First, the covariance between measurements in the same profile is estimated and decomposed into functional principal components (FPCs). Next, each profile is summarized using the first K principal components, and the resulting scores are used to estimate a space-time covariance model. Lastly, we estimate the remaining variance of the residuals not explained by the first K

components. As in [Kuusela and Stein \(2018\)](#), locally-estimated space-time covariance models are used to perform kriging and obtain the uncertainty in the estimates. This approach provides a computationally tractable way to predict a functional estimate that takes into account dependence in pressure.

In addition to providing estimates continuously at any pressure, the functional data approach can provide novel ways to estimate the properties of the resulting functions of temperature and salinity. We describe a general framework for their estimation with uncertainty measures and consider two applications to scientific problems where estimates are currently obtained discretely. First, we estimate the integrated ocean heat content at each location, which is related to the integral of the temperature curve. For the second application, the shape of the functional predictions is used to estimate the depth of the *mixed layer* of the ocean, a region directly below the ocean surface where the ocean mixes uniformly and is characterized by near-constant ocean properties (Sections 4.2 and 7.4 of [Talley et al., 2011](#)). The mixed layer drives the ocean-atmosphere interactions and thus influences heat and carbon flux of the ocean, ocean circulation, and biological processes dependent on light ([Holte et al., 2017](#)). Our functional estimates provide mixed layer depth estimates over all open oceans for each year that have minimal discretization error in pressure. These are only two of many potential applications of functional-data techniques addressing scientific questions using the Argo data.

We outline the rest of the paper, which loosely follows the structure of the introduction. In Section 2, the Argo data is introduced in more detail. In Section 3, we develop our approach for mean estimation and its computations, and apply it on the Argo data. This is *Stage I* of our analysis. In *Stage II*, after subtracting the mean from the data, we estimate the covariance of the residuals, predict using the estimated covariance, and assess the quality of our predictions in Section 4. In Section 5, a framework to use the functional estimates is developed, and two specific examples are given. Throughout our analysis, we provide the resulting estimates as data products to the community and introduce interactive R Shiny web applications for visualizing the results. We conclude and identify future research directions in Section 6.

2. Argo Data and Existing Methodologies. In this section, we give a more detailed overview of the Argo data and introduce two existing mapping approaches in oceanography. While there is a variety of measurements of the oceans, including sea surface temperature and ship-based measurements, we only use data from the Argo project because it provides a natural comparison to existing approaches.

2.1. Data from the Argo Project. The Argo program is an international collaboration that develops and manages floats, mechanical devices that collect measurements on the world's oceans ([Argo, 2000](#)). The Argo project reached a goal of global coverage in late 2007 and has continued to increase the number of floats to nearly 4,000 today; see, e.g., Figures 1 and 2 or a Shiny application in the Appendix A.2 for examples of the data. In ten-day cycles, each float descends from its parking depth at 1,000 dbar to a depth of 2,000 dbar, then rises over the course of six hours to the surface, collecting measurements of pressure, temperature, and salinity. Upon surfacing, the float transmits the data via satellite. The pressure, temperature, and salinity data and its associated location and time for each cycle is called a profile.

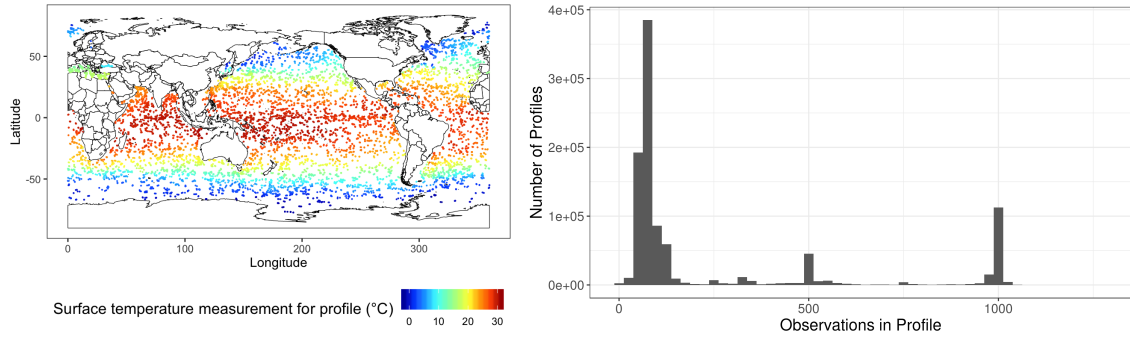


FIG 1. *Argo data examples. (Left) Locations of profiles collected in February 2016, colored by the temperature of the measurement closest to the surface. (Right) Histogram of the number of measurements per profile.*

The Argo program was designed to sample approximately one profile every 10 days in each 3 by 3 degree region of the open oceans. In terms of coverage of the oceans and the depth of measurements, the Argo project provides a wealth of data previously unavailable to oceanographers. While sea surface temperature can be measured at high spatial resolution through satellite, measurements at greater depths must be sampled in-situ. Before the Argo project, sampling at greater depths was sparse and highly nonuniform in space and time, with fewer measurements in the Southern Hemisphere and during winter months (Roemmich and Gilson, 2009).

The pressures at which each float samples can vary from float to float as well as from profile to profile. For example, floats developed earlier in the Argo project tended to sample sparsely, with the number of measurements per profile (around 50 to 200), due to data transmission technology at the time. Newer floats generally sample approximately every thirty seconds in time, then average these dense measurements to report about 1,000 measurements per profile to the satellite; see Figure 1. These two sampling schemes correspond to the “sparse” and “dense” functional data regimes studied by, for example, Li and Hsing (2010) and Zhang and Wang (2016). We treat the data from both regimes identically as samples at fixed pressures.

The Argo data are publicly available in a variety of forms, including monthly snapshots of the Global Data Assembly Center databases, `ftp` access, and `rsync` (Argo, 2000). The Argo data goes through automatic checks after transmission to satellite and is made available as real-time data within approximately 24 hours. Profiles also go through extended checks for data quality, after which the data is considered delayed-mode data. These checks can take 6 months and are especially important for the salinity data. For our analysis, we use a preprocessed version of the Argo data which was used in Kuusela and Stein (2018). In this version, profiles that do not meet their strict data quality checks are removed as detailed in their supplement. The data spans the years 2007 to 2016 based on the May 2017 snapshot of the Argo data. The data includes more than 245 million total point measurements from 994,709 profiles, of which 551,536 are high-quality delayed-mode profiles. Throughout our analysis, we generally use all profiles for temperature and only delayed-mode profiles for salinity, because salinity requires strict quality control described in Owens and Wong (2009).

2.2. *Argo Mapping Methodology.* Argo data is widely used in oceanography for both regional and global analyses of temperature and salinity. In this section, we review the important work of [Roemmich and Gilson \(2009\)](#), who provide a methodology for mean estimation and analysis of anomalies using the Argo data, as well as [Kuusela and Stein \(2018\)](#), who focus on covariance estimation and introduce maximum likelihood estimation for its model parameters in space and time. The Roemmich and Gilson product is available as the standard in global oceanography analysis using the Argo data. This product provides estimates of the mean temperature and salinity separately, as well as monthly anomalies from the mean over grids of different resolutions in space and fixed pressure levels. Before estimation, the temperature and salinity for each profile is interpolated onto 58 fixed nonuniformly-spaced pressure levels. Throughout, they use a distance based on latitude, longitude, and the depth of the ocean floor at each location. The inclusion of the depth of the ocean floor better handles areas where ocean currents run along the shores of continents like the Western boundary currents (see, for example, Section 7.8 of [Talley et al., 2011](#)). To estimate the mean, for each pressure level and grid point of space, they combine data from the years 2004-2016, using the 100 nearest profiles from each of the twelve months of the year. In addition, they only use the interpolated values at a pressure level as well as the two adjacent pressure levels. A weighted least squares approach based on distance from the grid point is used to fit a model of the form:

$$(2) \quad \beta_0 + \beta_1(s_{i1} - s_{01}) + \beta_2(s_{i2} - s_{02}) + \beta_3(s_{i1} - s_{01})^2 + \beta_4(s_{i2} - s_{02})^2 \\ + \beta_5(p_i - p_0) + \beta_6(p_i - p_0)^2 + \sum_{k=1}^6 \gamma_k \sin\left(\frac{d_i 2\pi k}{365.25}\right) + \sum_{k=1}^6 \delta_k \cos\left(\frac{d_i 2\pi k}{365.25}\right)$$

where s_{i1} and s_{i2} give the location of profile i , p_i the pressure level of the interpolated measurement, d_i is the day of the year profile i was observed, and β_k , γ_k , and δ_k are scalar coefficients. The coefficient β_0 represents the time-averaged mean, while the γ_k , and δ_k give the deviations from this mean at different times of the year. Overall, this approach is a form of local regression, where the time dimension is estimated using a fixed Fourier basis.

After subtracting the mean, Roemmich and Gilson then provide a field of anomalies for each month of each year that describes the variation away from the mean at a particular location. These are formed by computing the conditional mean at each grid point in space and pressure level assuming Gaussianity and using a covariance of the form

$$(3) \quad C_{RG}(\Delta_{RG}) = 0.77 \cdot \exp\left(-(\mathbf{a}^\top \Delta_{RG}/140)^2\right) + 0.23 \cdot \exp\left(-|\mathbf{a}^\top \Delta_{RG}|/1111\right)$$

Here, $\Delta_{RG} = (\Delta_{s_1}, \Delta_{s_2}, \Delta_{dep})^\top$ denotes a vector of distances between two locations s and s' for the zonal direction (East-West), meridional direction (North-South), and the distance penalty for ocean depth described above. The vector \mathbf{a} scales the relative directions and is $(1, 1, 1)$ above 20 degrees North and below 20 degrees South, but changes linearly to $(.25, 1, 1)$ at the equator, which increases the covariance in the zonal direction in the tropics. This choice is supported by empirical estimates near the surface. This covariance is nonstationary due to its dependence on \mathbf{a} , though the covariance does not depend on time or the pressure level. To form the final product, the anomalies over all months and years are averaged and added to the mean.

Kuusela and Stein (2018) employ the Roemmich and Gilson mean and study the covariance structure in more detail by proposing a space-time covariance model and fitting it using maximum likelihood. To address the nonstationarity of the data, they use the *locally stationary* assumption; that is, at each location, parameters of a stationary covariance are estimated using data nearby, and the local covariance estimates are used for prediction at that location. Data from different years are assumed independent, and one stationary covariance function for data observed in the same year they consider is

$$C_{KS}(\Delta_{KS}) = \phi \cdot \exp\left(-\sqrt{\frac{\Delta_{s_1}^2}{\theta_{s_1}^2} + \frac{\Delta_{s_2}^2}{\theta_{s_2}^2} + \frac{\Delta_d^2}{\theta_d^2}}\right) + \sigma^2 \cdot 1(\Delta_{KS} = 0)$$

where $\Delta_{KS} = (\Delta_{s_1}, \Delta_{s_2}, \Delta_d)^\top$ is the relevant distance between two locations and times in longitude, latitude, and day of the year, respectively. The estimated parameters are the process variance ϕ , nugget variance σ^2 , and three scale parameters θ subscripted by their direction. Thus, since the model is estimated at each pressure level, it can adapt to the large differences in the covariance structure at different depths. Furthermore, the model provides uncertainty for the estimates, which are validated using cross validation for both Gaussian and t-distributed errors. At many depths, the residuals may have non-Gaussian features as noted in Kuusela and Stein (2018). To further address this issue, Bolin and Wallin (2019) explore a class of multivariate non-Gaussian spatial models that offer some improvements in prediction on a limited analysis of Argo data.

3. Functional Mean Estimation for Argo Data. In this section, we introduce our functional approach for mean estimation, in which we estimate a smooth function $\mu(s_0, d_0, y, p_{i,j})$ for a location s_0 . In particular, consider the class of functions

$$\mathbb{W}_2 = \left\{ f \mid f^{(2)} \text{ exists almost everywhere, and } \int_0^{2000} (f^{(2)}(p))^2 dp < \infty \right\}$$

where $f^{(k)}$ is the k th derivative of f . The space \mathbb{W}_2 is a Sobolev space of functions widely used for nonparametric inference including problems in FDA (Hsing and Eubank, 2015; Wahba, 1990). The size of $\|f^{(2)}\|_{\mathbb{L}_2}^2 = \int (f^{(2)}(p))^2 dp$ quantifies the smoothness of f , i.e., if $\int (f^{(2)}(p))^2 dp = 0$, then f takes the form of a line.

3.1. *A Functional Approach to Mean Estimation.* We consider a mean estimated locally in space and day of the year which can be evaluated at any pressure in $[0, 2000]$. Our novel approach combines local regression (to smooth space and time) and smoothing splines (to smooth pressure) by estimating the function:

$$(4) \quad f_\beta(s_i, d_i, y_i, p) = \sum_{y=2007}^{2016} \beta_{0,y}(p)1(y_i = y) + (s_{1i} - s_{10})\beta_1(p) + (s_{2i} - s_{20})\beta_2(p) + (s_{1i} - s_{10})^2\beta_3(p) + (s_{2i} - s_{20})^2\beta_4(p) + (s_{1i} - s_{10})(s_{2i} - s_{20})\beta_5(p) + (d_i - d_0)\beta_6(p) + (d_i - d_0)^2\beta_7(p)$$

where $s_0 = (s_{10}, s_{20})$ is a fixed location and d_0 is a fixed day of the year. We also include the standard smoothing spline penalty on the second derivative of each function:

$$\text{Pen}(\lambda) = \lambda_0 \sum_{y=2007}^{2016} \left\| \beta_{0,y}^{(2)} \right\|_{\mathbb{L}_2}^2 + \sum_{k=1}^7 \lambda_k \left\| \beta_k^{(2)} \right\|_{\mathbb{L}_2}^2$$

where the λ_j are nonnegative smoothing parameters. This penalty controls the smoothness of the estimated functions. With this notation, for a fixed location s_0 we solve the optimization problem:

$$(5) \quad \min_{\beta_k \in \mathbb{W}_2} (\ell(\beta) + \text{Pen}(\lambda)),$$

where

$$(6) \quad \ell(\beta) = \frac{1}{n} \sum_{i=1}^n \frac{K_{h_s, h_d}(s_i - s_0, d_i - d_0)}{m_i} \left\| \Sigma_i^{-\frac{1}{2}} (Y_i - f_{\beta,i}) \right\|_2^2,$$

and Y_i and $f_{\beta,i}$ are vectors with entries $\{Y_{i,j}\}_{j=1}^{m_i}$ and $\{f_{\beta}(s_i, d_i, y_i, p_{i,j})\}_{j=1}^{m_i}$, respectively. Here, K_{h_s, h_d} is a product of Epanechnikov kernels, the first based on the great-circle distance between s_i and s_0 with bandwidth h_s and the second based on the difference in day of the year between d_i and d_0 with bandwidth h_d . This type of kernel is commonly used for local regression (Fan and Gijbels, 1996). Also, Σ_i is a matrix that specifies the working correlation between measurements in the same profile; we address choosing its form in the next section. Dividing by m_i in (5) ensures that profiles with more measurements do not contribute in greater proportion to the loss function compared to profiles with fewer measurements. We propose this new general nonparametric approach of combining local regression and spline smoothing for estimating a spatially-varying functional mean.

The optimization problem (5) is solved for temperature and salinity separately. The functions $\beta_{0,y}$ for $y = 2007, \dots, 2016$ give a mean function estimated from each year. The function $\bar{\beta}(p) = \frac{1}{10} \sum_{y=2007}^{2016} \beta_{0,y}(p)$ is the year-averaged mean at s_0 and d_0 . The additional functions β_1 through β_7 are used to estimate the derivatives of the mean with respect to space and time, for each pressure. Figure 2 gives results at one location in the Pacific Ocean for the first 350 dbar with $d_0 = 45.25$, corresponding the mid-February. The mean functions are able to capture the constant temperature near the surface known as the mixed layer, which we address in more detail in Section 5. The reader can compute (5) for fixed smoothing parameters using an R Shiny application in the Appendix A.2.

3.2. Computation and Cross Validation. In this section, we give an overview of our approach for computation and how to choose smoothing parameters. More details are shown in the Appendix A.3. The solution to (5) must be computed for each location of interest s_0 ; however, calculations for different s_0 do not rely on each other, so they can be easily made in parallel over multiple computer cores. By applying Theorem 6.6.9 of Hsing and Eubank (2015) to losses that include multiple functions in \mathbb{W}_2 , we obtain that each function of the resulting solution to the infinite dimensional optimization problem (5) is a natural cubic spline with knots at each uniquely observed $p_{i,j}$ for each i such that $K_{h_s, h_d}(s_i - s_0, d_i - d_0) > 0$. In practice, a nearly exact solution is defined using penalized cubic B-splines

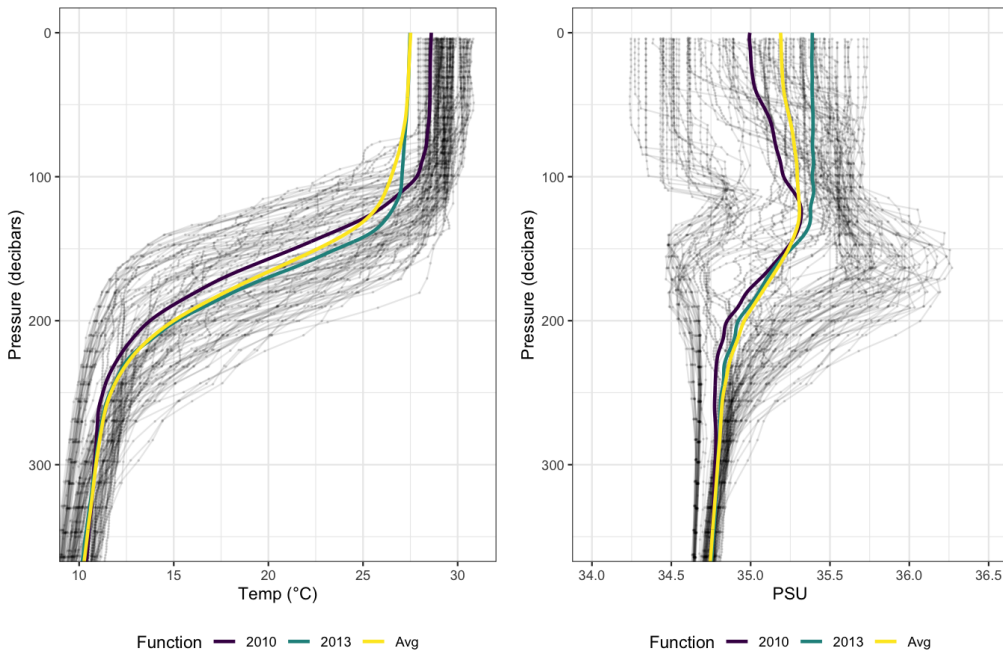


FIG 2. Data used from 2010 for first 350 dbar for $-170.5^\circ W$ $0.5^\circ N$, $d_0 = 45.25$ for **(Left)** temperature ($^\circ C$) and **(Right)** salinity (practical salinity units, PSU). We plot the estimated mean functions $\beta_{2010}(p)$ and $\beta_{2013}(p)$ for two of the years and the year-averaged estimate $\beta(p)$. In this figure as well as Figures 5 and 8 we plot according to the oceanography convention with pressure on the y axis in reference to depth in the ocean.

bases with 200 equispaced knots in $[0, 2000]$. Placing a knot at each observed pressure value is prohibitively costly when a large number of profiles are included in each fit. Our experiments with a reduced set of computations indicate that the difference with the exact solution involving knots at all relevant pressures is small, and this basis provides knots at intervals near the size of Argo pressure uncertainties of ± 2.4 dbar. Due to the local nature of the B-splines, the relevant matrices needed to compute the solutions are sparse and banded, which leads to further computational gains. In particular, the Cholesky decomposition of matrices is numerically efficient in computing the solution. To compute the B-spline basis functions and penalty, we use the `fda` package, and we have implemented a quicker version of the `eval.basis` for the evaluation of the basis functions.

In addition to computing the solution, we also need to choose the smoothing parameters λ_j and bandwidths h_s and h_d . Smoothing parameters λ_j are currently chosen assuming h_s and h_d fixed. We set $h_s = 900$ kilometers for both temperature and salinity and $h_d = 45.25$ days. This provides nearly enough profiles for each grid point and year and uses data from three months of the year. Also, if fewer than 10 profiles were used for each year, h_s is increased so that there are at least 10 profiles used for each year. To choose λ_j , we use generalized cross validation (GCV) for its favorable properties, ease of calculation, and ability to include a correlation structure in the choice of λ (Wahba, 1990). The GCV score

in the context of our problem is

$$\text{GCV}(\lambda) = \frac{(Y - \hat{Y})^\top \Sigma^{-1} (Y - \hat{Y})}{(1 - \text{tr}(A(\lambda))/n_{s_0})^2}$$

where $n_{s_0} = \sum_{i=1}^n 1(K_{h_s, h_d}(s_i - s_0, d_i - d_0) > 0) m_i$, $A(\lambda)$ is the ‘‘hat’’ matrix defined in the Appendix A.3, Y are the observations for temperature or salinity, \hat{Y} are predictions using smoothing parameters λ , and Σ^{-1} is the block-diagonal matrix

$$\Sigma^{-1} = \text{diag} \left[\frac{K_{h_s, h_d}(s_i - s_0, d_i - d_0)}{nm_i} \Sigma_i^{-1}, i = 1, \dots, n \right].$$

Considering approaches like variable bandwidth selection, jointly choosing bandwidths and smoothing parameters, and leave-one-profile-out cross validation are methodological and computational challenges that can motivate further research.

Computing the leverage scores for the calculation of GCV is the largest computational cost in the selection of λ . There are algorithms for the efficient computation of the leverage scores when the matrices Σ_i^{-1} are diagonal (Hutchinson and de Hoog, 1985). However, using a working correlation matrix results in a matrix that is no longer banded, but still very sparse. We apply the related algorithm for the computation of the leverage scores for general sparse matrices based on the Cholesky decomposition (Erisman and Tinney, 1983) and thus avoid the full inversion of matrices. These are implemented as a Matlab module and made available in R (Davis, 2006; Zammit-Mangion, 2018). For choosing multiple smoothing parameters, computing the GCV function on a two-dimensional or larger grid becomes prohibitively expensive. We have taken the approach of finding suitable fixed ratios $\eta_\ell = \lambda_\ell/\lambda_0$ for each ℓ , then using the smoothing parameters $a\eta$ and cross validating on the single parameter $a > 0$. These ratios are chosen to balance the units of each of the covariates, and the quadratic terms require larger amounts of smoothing. In particular, we let $\eta = (1, 10^8, 10^8, 10^{13}, 10^{13}, 10^{13}, 10^9, 10^{13})$ and conduct standard 1-d optimization using `optimize` in R to search for $a \in (10^{-3}, 10^7)$.

Loosely choosing the working correlation structure Σ_i improves the quality of cross validation and solution functions. A simple choice employed here is Markovian-type dependence in continuous pressure. Specifically, we consider $(\Sigma_i)_{j,k} = \exp(-\tau|p_{i,j} - p_{i,k}|)$ with $\tau \in (0, \infty)$, resulting in a tridiagonal precision matrix Σ_i^{-1} . In practice, we have found that using this within-profile correlation with $\tau = 0.001$, which corresponds to a correlation of about 0.9512 for measurements 50 dbar apart, helps both the selection of λ as well as the quality of solution. In Section 4, the within-profile covariance is estimated, and in Appendix A.5 it is shown that the empirical covariance estimates generally match well with this choice. One could include a non-constant working variance as well, though such benefit may be marginal.

We compute the solution to (5) in R on a 1 degree by 1 degree grid in space for mid-February ($d_0 = 45.25$) between -80° S and 80° N. This results in 47,938 and 46,023 grid points computed for temperature and salinity, respectively. For salinity, we use only delayed-mode data. For each profile i from the first three months of the year, residuals were computed by using the mean estimate at the nearest grid point to profile i as $Y_{i,j} - \hat{f}_\beta(p_{i,j})$. The implicit assumption of computing these residuals is that the mean is represented well by a locally quadratic function of day of the year for these three months as in (4).

3.3. *Functional Derivatives.* One novelty in our approach of combining local regression and spline smoothing is its estimation of functional derivatives. Namely, writing the mean averaged over years as $\bar{\mu}(s, d, p)$, the functions $(\hat{\beta}_1(p), \hat{\beta}_2(p))$ estimate

$$\left(\frac{\partial \bar{\mu}}{\partial s_1}(s, d, p), \frac{\partial \bar{\mu}}{\partial s_2}(s, d, p) \right),$$

the gradient consisting of the partial derivatives at $s = s_0$ and $d = d_0$ of the response with respect to zonal distance and meridional distance, respectively. Likewise, $(2 \cdot \hat{\beta}_3, 2 \cdot \hat{\beta}_4, \hat{\beta}_5)$ estimate the second-order derivatives

$$\left(\frac{\partial^2 \bar{\mu}}{\partial s_1^2}(s, d, p), \frac{\partial^2 \bar{\mu}}{\partial s_2^2}(s, d, p), \frac{\partial^2 \bar{\mu}}{\partial s_1 \partial s_2}(s, d, p) \right),$$

and $(\hat{\beta}_6, 2 \cdot \hat{\beta}_7)$ estimate

$$\left(\frac{\partial \bar{\mu}}{\partial d}(s, d, p), \frac{\partial^2 \bar{\mu}}{\partial d^2}(s, d, p) \right)$$

at the location and time $s = s_0$ and $d = d_0$. These functions collectively describe the local quadratic behavior of the mean near s_0 and d_0 . In Figure 3, the derivatives in latitude and time for temperature are given for a cross-section of the ocean for a fixed longitude. Also, the figure includes the direction and strength of the spatial gradient at a fixed pressure of 10 dbar for salinity. These derivatives can identify the direction of warming and cooling for each location and pressure, as well as physical properties including the exchange of salty and fresh waters near the Strait of Gibraltar. Our functional approach facilitates this detailed description of the ocean properties at any pressure.

3.4. *Comparison with Roemmich and Gilson (2009).* In this section, we compare and contrast our mean estimation approach with the excellent oceanographic standard for the Argo data due to Roemmich and Gilson (2009). While Roemmich and Gilson (2009) treats years equally and uses data from the entire year simultaneously, we use data from only the first three months of the year and model the variation across years. Accounting for the changes in ocean properties from year to year changes the structure of the residuals, especially near the ocean surface. This mean estimation approach differs from the standard approach in oceanography, where the mean field often is an average over all years, and the deviation from this mean is studied separately and referred to as the ‘‘anomaly.’’ Estimating these anomalies gives a natural way to compare conditions from different years. From a statistical perspective, this approach leads to a challenge, since the yearly variation can overwhelm the spatio-temporal variability in the residuals. For example, in Kuusela and Stein (2018), the scale parameters for longitude and latitude in the covariance models near the ocean surface are often on the scale of thousands of kilometers. Such large-scale covariance models are likely artefacts of the presence of anomalies, which we claim can be better captured in the mean rather than the covariance component of the model. Modeling the year-to-year variation in the mean decreases the range of dependence for the resulting residuals. This makes our functional covariance modeling easier by ensuring that the resulting

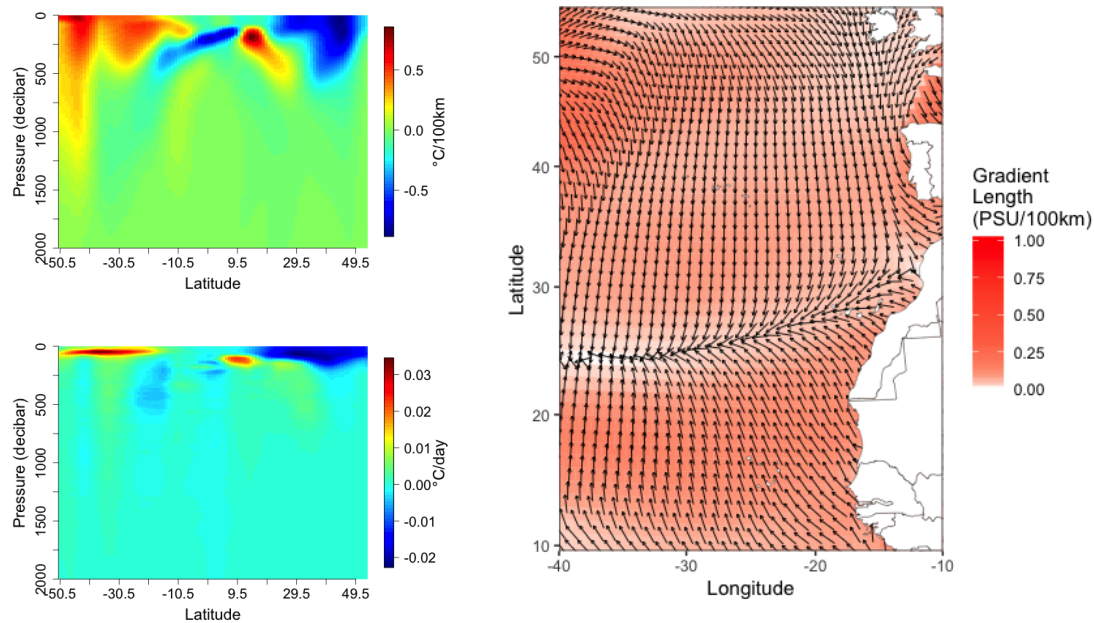


FIG 3. Estimates of derivatives of temperature in latitude (**Top Left**) and time (**Bottom Left**) for a fixed longitude 179.5 West. The derivative with respect to latitude reflects that in the middle latitudes (between (30, 50) and (-50, -30)) the temperature increases as one moves towards the equator near the surface. The derivatives also identify two separate areas of high temperature on either side of the equator near 250 dbar. The derivative with respect to time demonstrates that in mid-February, the temperature is mostly increasing in the Southern Hemisphere and mostly decreasing in the Northern Hemisphere as the time of year suggests. On the right, we give the gradient in space in PSU per 100 km for salinity at 10 dbar in mid-February (**Right**). The gradient points toward the salinity maximum in the Central North Atlantic, identifies the flow of salty water from the Mediterranean Sea, and shows accordance with [Talley et al. \(2011\) Figure 4.15](#) that gives the distribution of sea-surface salinity in the oceans in Jan-March.

residuals have zero mean for each local fit for each year. After modeling the covariance, the predictions are more closely compared with [Kuusela and Stein \(2018\)](#) in Section 4.5.

There are additional differences between the two approaches for mean estimation, mainly in the data used. The Roemmich and Gilson mean uses additional data from 2004 to 2006 and less stringent data quality checks that require more care. In addition, we use a fixed kernel bandwidth rather than the nearest 100 profiles from each of the 12 months. Our year-averaged mean for mid-February is compared with the Roemmich and Gilson mean in mid-February in Figure 4 for one pressure level. Detailed comparisons at additional pressure levels are available using an R Shiny application detailed in the Appendix A.2. The mean fields were kindly provided by John Gilson. In general, there are two notable differences in the estimates when comparing the two fields. In the Western boundary currents, the fields differ likely due to the distance metrics used; since Roemmich and Gilson account for differences in the depth of the ocean in the distance metric, they employ more data along the coasts compared to our estimates. Our mean is more smooth in space since we choose a large bandwidth, and more of the spatial variability is modeled through the covariance.

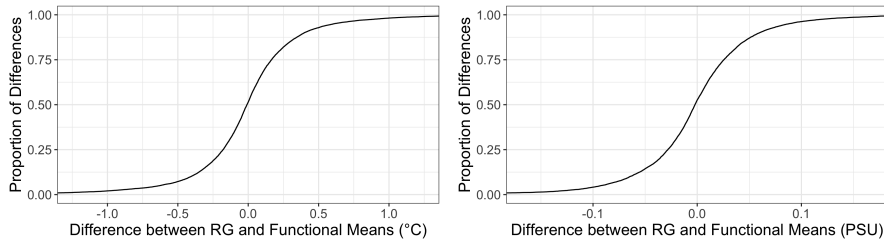


FIG 4. Empirical cumulative distribution functions of Roemmich-Gilson mean estimates minus functional mean estimates at 300 dbar for (Left) temperature and (Right) salinity over each grid point. Both means refer to mid-February, and most differences are less than .5 degrees Celsius and 0.1 PSU.

4. Covariance Estimation. After subtracting the mean from the data, the spatial dependence structure of the residuals can be modeled to provide predictions and estimate uncertainties. Modeling the covariance in space, time, and pressure is a challenging task. For example, there are considerable differences in the spatial dependence structure and residual variances at different pressures and locations.

Our covariance estimation can be described in three steps. First, we estimate the functional principal components (FPCs), which explain the first few dimensions of variability in pressure (cf. Hsing and Eubank, 2015, Chapter 9). Next, each profile is summarized by these principal components, and the resulting scores are modeled. Lastly, we estimate the remaining variability not accounted for by the principal components. The implicit assumptions in this approach are that the covariance structure of temperature and salinity changes smoothly as a function of pressure and only a small number of FPCs are needed to approximate the spatial and temporal structure in pressure.

We develop this approach in mathematical notation first by assuming

$$(7) \quad Y_{i,j}^0 = X(s_i, d_i, y_i, p_{i,j}) + \epsilon_{i,j}$$

where $\{Y_{i,j}^0\}_{j=1}^{m_i}$ are the residuals for profile i formed by subtracting the mean estimate from the data, $X(s, d, y_i, \cdot)$ for $y_i = 2007, \dots, 2016$ are identically-distributed realizations of a functional random field with mean 0, and $\epsilon_{i,j}$ is measurement error with mean 0 and finite variance that may depend on pressure. If $X(s_i, d_i, y_i, \cdot) \in \mathbb{L}_2$ for each s_i and d_i , one can write

$$X(s_i, d_i, y_i, p) = \sum_{k=1}^{\infty} Z_k(s_i, d_i, y_i) \phi_k(p)$$

where ϕ_k are fixed orthonormal functions, and the $Z_k(s, d, y)$ are scalar random fields that are weakly dependent in time that we refer to as *scores*. This is similar to the Karhunen-Loève expansion for zero-mean square-integrable stochastic processes, though the scores may be correlated across k due to their spatial dependence. In the subsequent development, we simplify the notation by defining $Z_{i,k} = Z_k(s_i, d_i, y_i)$ where it does not cause confusion. For an adequate choice of ϕ_k , we would expect that $X(s_i, d_i, y_i, \cdot)$ can be approximated as

$$(8) \quad X(s_i, d_i, y_i, p) = \sum_{k=1}^{K_1} Z_{i,k} \phi_k(p)$$

for some small number K_1 . This effectively reduces the dimension of our problem. Here, each ϕ_k is a fixed function that has been estimated through some form of functional principal component analysis, with one such approach given in Section 4.1. For a choice of ϕ_k and a profile i , the scores are estimated by the least squares solution

$$(9) \quad Z_{i,\cdot} = \left(\Phi_i^\top \Phi_i \right)^{-1} \Phi_i^\top Y_i^0$$

where Y_i^0 is the residuals for profile i and $\Phi_i \in \mathbb{R}^{m_i \times K_1}$ is the matrix with j, ℓ entry $\phi_\ell(p_{i,j})$. The principal component functions ϕ_k and the scores $Z_{i,\cdot}$ are only estimates and not the truth, though we use the same notation for convenience.

We assume that the decomposition (8) of $X(s_i, d_i, y_i, p)$ holds locally with respect to both $Z_{i,k}$ and ϕ_k , similar to the locally stationary assumption of Kuusela and Stein (2018). That is, for a fixed location s_0 and time d_0 , the functions ϕ_k are estimated and used to form estimates of the $\{Z_{i,k}\}_{k=1}^{K_1}$ and the measurement error variance $\kappa(p) := \kappa(s_0, d_0, p)$ for all nearby profiles. Next, the distribution of the nearby scores are modeled. For different choices of (s_0, d_0) , the functions ϕ_k and resulting scores $\{Z_{i,k}\}_{k=1}^{K_1}$ and nugget variance $\kappa(p)$ are different.

The model gives a clear approach to address the fundamental problem of functional kriging, i.e. spatial prediction, using the conditional distribution at an unobserved location given the data observed. For any set of data Y^0 , to provide a prediction for the function-valued random field $X(s_*, d_*, y, \cdot)$ for an unobserved location s_* at time d_* , one has

$$(10) \quad \mathbb{E} \{X(s_*, d_*, y, p) | Y^0\} = \phi(p)^\top \mathbb{E} \{Z.(s_*, d_*, y) | Y^0\}$$

$$(11) \quad \text{Var} \{X(s_*, d_*, y, p) | Y^0\} = \phi(p)^\top \text{Var} \{Z.(s_*, d_*, y) | Y^0\} \phi(p)$$

where $\phi(p) = (\phi_1(p), \phi_2(p), \dots, \phi_{K_1}(p))^\top$ are the principal components and $Z.(s_*, d_*, y) = (Z_1(s_*, d_*, y), \dots, Z_{K_1}(s_*, d_*, y))^\top$ are the scores of $X(s_*, d_*, y, \cdot)$. Furthermore, for each residual point $Y_{i,j}^0$,

$$(12) \quad \mathbb{E} \{Y_{i,j}^0 | Y^0\} = \mathbb{E} \{X(s_i, d_i, y_i, p_{i,j}) | Y^0\}$$

$$(13) \quad \text{Var} \{Y_{i,j}^0 | Y^0\} = \text{Var} \{X(s_i, d_i, y_i, p_{i,j}) | Y^0\} + \kappa(p_{i,j})$$

Thus, if one assumes that the field of $\{Z_k(s, d, y); k = 1, \dots, K_1; (s, d) \in \mathbb{R}^3\}$ is Gaussian, one only needs a spatio-temporal model of the scores $Z_k(s, d, y)$ for $k = 1, \dots, K_1$ using the conditional mean and variance, as well as estimate $\kappa(p)$. We address the estimation of $\phi_k(p)$ in Section 4.1, the modeling of the scores $Z_{i,k}$ in Section 4.2, and the estimation of $\kappa(p)$ in Section 4.3.

4.1. *Marginal Covariance Estimation in Pressure.* In this section, we focus on the estimation of ϕ_k in (8), which amounts to performing local functional principal component analysis (FPCA). A fixed set of basis functions may not be suitable for different parts of the ocean or different seasons, and we thus estimate ϕ_k locally in space and time as done with the mean. One could also use a fixed set of functions ϕ_k over all locations, though the resulting decomposition would be suboptimal at most or all locations compared to the local principal component decomposition. At each location, a local version of the approach

given in Section 8.3 of [Hsing and Eubank \(2015\)](#) is used to estimate the entire within-profile covariance. Then, the covariance is decomposed to obtain the functional principal components. This approach uses data from both sparse and dense profiles and does not depend on a basis representation of each profile as in [Ramsay and Silverman \(2013\)](#). Also, it is similar to our approach for mean estimation by treating the covariance as an expectation, and it provides advantages over other approaches like thin plate splines by using B-splines that greatly reduce computations ([Wahba, 1990](#)).

For a fixed s_0 and d_0 , we solve the optimization problem:

$$(14) \quad \min_{f \in \mathbb{W}_2 \otimes \mathbb{W}_2} (\ell(f) + \text{Pen}_f(\lambda))$$

where

$$(15) \quad \ell(f) = \frac{1}{n} \sum_{i=1}^n \frac{K_{h_s, h_d}(s_i - s_0, d_i - d_0)}{m_i(m_i - 1)} \sum_{1 \leq j \neq k \leq m_i} (Y_{i,j}^0 Y_{i,k}^0 - f(p_{i,j}, p_{i,k}))^2.$$

In particular, f is restricted to be of the form

$$f(p_1, p_2) = \sum_{k_1=1}^M \sum_{k_2=1}^M \alpha_{k_1, k_2} \chi_{k_1}(p_1) \chi_{k_2}(p_2)$$

where $\{\alpha_{k_1, k_2}\}_{k_1, k_2=1}^M$ are scalar coefficients and $\{\chi_k(p)\}_{k=1}^M$ is a univariate B-spline basis over a fixed set of knots. As suggested in [Wood \(2006\)](#), the penalty used is

$$\text{Pen}_f(\lambda) = \lambda \text{vec}(\alpha)^\top (\Omega \otimes I_M + I_M \otimes \Omega) \text{vec}(\alpha)$$

where \otimes is the standard Kronecker product, Ω is the univariate smoothing matrix for the B-splines used with k_1, k_2 entry $\int_0^{2000} \chi_{k_1}^{(2)}(p) \chi_{k_2}^{(2)}(p) dp$, and I_M is the $M \times M$ identity matrix. This penalty approximates

$$\lambda \int_0^{2000} \int_0^{2000} \left[\left(\frac{\partial^2 f}{\partial p_1^2} \right)^2 + \left(\frac{\partial^2 f}{\partial p_2^2} \right)^2 \right] dp_1 dp_2$$

as given in [Wood \(2006\)](#). The computation is similar to the approach for mean estimation, with λ chosen by cross validation and using a product kernel with $h_s = 550$ kilometers and $h_d = 45.25$; this smaller spatial bandwidth is possible since we pool together data from all years. One additional challenge is that the inner sum in (15) becomes too large since $m_i(m_i - 1) \approx 10^6$ for some profiles. Thus, for each profile such that $m_i > 50$, we randomly select 50 observations to use in the fit, which effectively makes $m_i(m_i - 1) \leq 2450$ for each i . We use $M = 102$ with equally spaced knots over $[0, 2000]$ for the basis χ_k . The overall size of the problem is M^2 , whose computational cost increases much faster compared to the mean estimation. This choice of knots is able to approximate the covariance operator reasonably well while ensuring the calculations are computationally manageable.

The main goal of the covariance estimation is to obtain a basis of functional principal components for the space-time modeling. To find the principal components, the $M \times M$ matrices B with entries $(B)_{k_1, k_2} = \alpha_{k_1, k_2}$ and a Gram matrix Ω_0 with entries $(\Omega_0)_{k_1, k_2} =$

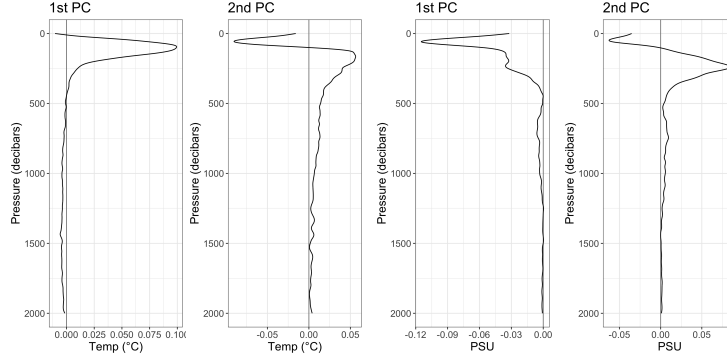


FIG 5. Example of first two estimated functional principal components (**Left**) temperature (**Right**) salinity at Long 90.5 W and Lat -10.5 S. The principal components suggest much higher variance near the surface of the ocean, as expected.

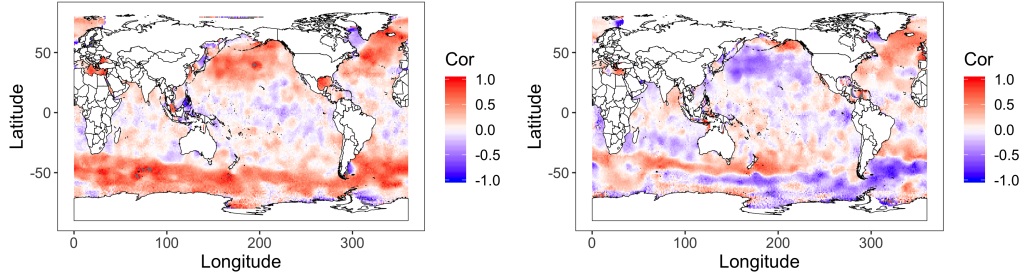


FIG 6. Estimated correlation between observations in the same profile at pressures of 10 and 800 dbar (**Left**) temperature (**Right**) salinity.

$\int_0^{2000} \chi_{k_1}(p)\chi_{k_2}(p)dp$ are formed. Then, performing standard principal components analysis on the matrix $\Omega_0^{1/2}B\Omega_0^{1/2}$ results in the vectors $\{v_1, v_2, \dots, v_M\}$, and the vectors $\{\Omega_0^{-1/2}v_1, \Omega_0^{-1/2}v_2, \dots, \Omega_0^{-1/2}v_M\}$ give the coefficients for the FPCs in the basis $\{\chi_k\}_{k=1}^M$. The use of Ω_0 rotates the problem into the space with the \mathbb{L}_2 inner product, decomposes the principal components in this space, then rotates the vectors back to the space of original coefficients. This ensures that the resulting functions are orthonormal with respect to the \mathbb{L}_2 inner product. At this point, we estimate the FPCs for temperature and salinity separately. By working in this basis for future modeling, we reduce the problem from an infinite-dimensional functional covariance operator in pressure to a low-dimensional subspace of principal components.

An example of the first two functional principal components for a location is shown in Figure 5. Similar plots for other locations can be viewed at on a R Shiny application given in the Appendix A.2. These principal components can give descriptive information on the variance and dependence of temperature and salinity with respect to pressure. There is evidence that the covariance and the principal components for temperature and salinity exhibit different structure. For example, in Figure 6, the estimated correlation of temperature is generally positive for measurements at 10 and 800 dbar, while at many locations, the estimated correlation of salinity is negative. This may reflect how the oceans can heat or

cool collectively while the overall amount of salinity in the ocean is relatively constant. We hypothesize that the boundary between negative and positive correlated measurements for salinity at these depths in the Southern Ocean roughly picks out the Subantarctic Front (SAF) (Talley et al., 2011, Chapter 13).

4.2. *Space-time modeling of scores.* In this section, we model the scores for spatio-temporal prediction. A simple approach would be to consider each of the scores independently and fit a univariate spatial model to each score separately. However, this implies some sort of weak separability in the covariance with respect to pressure and space (Lynch and Chen, 2018). This assumption may not be satisfied for the Argo data, since one set of principal components may not best represent all profiles within a spatial area and the dependence with respect to space, time, and pressure may not be separable. In addition, to jointly model temperature and salinity, we must take into account their dependence. These two challenges motivate an initial decorrelation step, after which the transformed scores are modeled independently.

Focusing on the estimation of the random, mean-zero function in (8), we write

$$T^0(s_i, d_i, y_i, p) = \sum_{k=1}^{K_1} Z_{i,k} \phi_k(p), \text{ and } S^0(s_i, d_i, y_i, p) = \sum_{k=1}^{K_2} W_{i,k} \psi_k(p),$$

where T^0 , $Z_{i,k} := Z_k(s_i, d_i, y_i)$, and ϕ_k denote the respective terms of (8) for temperature, and S^0 , $W_{i,k} := W_k(s_i, d_i, y_i)$, and ψ_k denote the terms for salinity. For the modeling, we adopt the locally stationary assumption of Kuusela and Stein (2018). For each location, as described in (9), we use the ϕ_k estimated at that location to estimate the temperature scores $Z_{i,k}$ for profiles within some radius of that location, and likewise use the respective terms for salinity, ψ_k to estimate $W_{i,k}$. For profiles that have very few measurements or the measurements do not span a large section of the pressure dimension, one cannot get a reasonable estimate for the scores, and these profiles are excluded. The goal of this section is to estimate a predictive distribution for the vector

$$\begin{pmatrix} Z_{*,\cdot} \\ W_{*,\cdot} \end{pmatrix} = (Z_{*,1}, Z_{*,2}, \dots, Z_{*,K_1}, W_{*,1}, W_{*,2}, \dots, W_{*,K_2})^\top,$$

at an unobserved location to jointly model temperature and salinity. We first introduce our decorrelation step as explained below.

For the modeling of the resulting scores, let Σ_{scores} be a $(K_1 + K_2) \times (K_1 + K_2)$ marginal covariance matrix of $\begin{pmatrix} Z_{i,\cdot}^\top \\ W_{i,\cdot}^\top \end{pmatrix}$. This matrix Σ_{scores} is estimated by

$$\hat{\Sigma}_{\text{scores}} = \frac{1}{|D_{s_0}| - 1} \sum_{i \in D_{s_0}} \begin{pmatrix} Z_{i,\cdot} \\ W_{i,\cdot} \end{pmatrix} \begin{pmatrix} Z_{i,\cdot}^\top & W_{i,\cdot}^\top \end{pmatrix}$$

where D_{s_0} are the set of nearby delayed mode profiles. Then, consider the standard eigen-decomposition

$$\hat{\Sigma}_{\text{scores}} = V \Gamma V^\top$$

where Γ is a diagonal matrix, and define

$$(16) \quad \begin{pmatrix} \tilde{Z}_{i,\cdot} \\ \tilde{W}_{i,\cdot} \end{pmatrix} = V^\top \begin{pmatrix} Z_{i,\cdot} \\ W_{i,\cdot} \end{pmatrix}.$$

The resulting transformed scores $\left(\tilde{Z}_{i,\cdot}^\top, \tilde{W}_{i,\cdot}^\top\right)^\top$ are then approximately decorrelated, with diagonal auto-covariance matrix Γ .

Let $M(\nu, \Delta) = c_1 \Delta^\nu \mathcal{K}_\nu(\Delta)$ be the Matérn covariance with parameter ν at distance Δ with unit variance and scale, studied in, for example, [Stein \(2013\)](#). Here, c_1 is a constant so that $M(\nu, 0) = 1$, and \mathcal{K}_ν is the modified Bessel function of the second kind. The value of $\nu > 0$ governs the smoothness of the field of scores, where larger values give a smoother field. When $\nu = 1/2$, the Matérn model reduces to the exponential function. In our experiments, the choice of ν had minimal effects on the resulting predictions, and we set it to the common choice $\nu = 1/2$ as in [Kuusela and Stein \(2018\)](#). For $\tilde{Z}_{i,k}$ and $\tilde{W}_{i,k}$ and each k , a Matérn model is fitted for the decorrelated scores of the form $\mathbb{E} \left(\tilde{Z}_{i,k} \tilde{Z}_{j,k} \right) = C_k(\Delta_{i,j})$ or $\mathbb{E} \left(\tilde{W}_{i,k} \tilde{W}_{j,k} \right) = C_{K_1+k}(\Delta_{i,j})$ if $y_i = y_j$ with

$$(17) \quad C_k(\Delta) = \gamma_k \cdot M \left(\nu, \sqrt{\left(\frac{\Delta_{s_1}}{\theta_{s_1,k}}\right)^2 + \left(\frac{\Delta_{s_2}}{\theta_{s_2,k}}\right)^2 + \left(\frac{\Delta_d}{\theta_{d,k}}\right)^2} \right) + \sigma_k^2 \cdot 1(\Delta = 0),$$

where $\Delta = (\Delta_{s_1}, \Delta_{s_2}, \Delta_d)$ is a vector of corresponding distances in space and time. The parameters $\theta_{s_1,k}$, $\theta_{s_2,k}$ and $\theta_{d,k}$ are scale parameters that specify the correlation ranges for each of the directions. Lastly, γ_k and σ_k^2 are parameters that describe the variance of the spatial process and the measurement error (nugget). This space-time model is considered in [Kuusela and Stein \(2018\)](#) in their fixed pressure level analysis.

In summary, the resulting covariance of temperature and salinity is

$$(18) \quad \mathbb{E} \left\{ \begin{pmatrix} T^0(s_i, d_i, y_i, p_1) \\ S^0(s_i, d_i, y_i, p_1) \end{pmatrix} \begin{pmatrix} T^0(s_j, d_j, y_j, p_2) \\ S^0(s_j, d_j, y_j, p_2) \end{pmatrix}^\top \right\} = \Xi_{p_2}^\top V C(\Delta_{i,j}) V^\top \Xi_{p_1}$$

if $y_j = y_i$ and 0 otherwise, where $C(\Delta_{i,j}) \in \mathbb{R}^{(K_1+K_2) \times (K_1+K_2)}$ is the diagonal matrix with the k -th element $C_k(\Delta_{i,j})$, and $\Xi_p = \begin{pmatrix} \phi(p) & 0 \\ 0 & \psi(p) \end{pmatrix} \in \mathbb{R}^{(K_1+K_2) \times 2}$.

We estimate the spatial model for February at each location using data from January, February, and March. For each location, profiles within 1,100 kilometers were used. This is similar to the size of the moving windows used in [Kuusela and Stein \(2018\)](#). We set $K_1 = K_2 = 10$, which allows the profiles to be well represented by the principal components, though our experiments suggest that more principal components may slightly improve predictions near the surface. To estimate the parameters γ_k , $\theta_{s_1,k}$, $\theta_{s_2,k}$, $\theta_{d,k}$, and σ_k^2 for each k , we employ the same approach as [Kuusela and Stein \(2018\)](#) using maximum likelihood summarized below. Let \tilde{Z}_y be the scores for one k for year y in each of the above models, and let $\text{Var}(\tilde{Z}_y) = \Sigma_y$ be a matrix specified by the parameters in (17) above. We assume that \tilde{Z}_y are multivariate Gaussian, so that the log likelihood of the data for all $y = 2007, \dots, 2016$

is

$$-\frac{1}{2} \left(\sum_{y=2007}^{2016} \log(\det(\Sigma_y)) + \tilde{Z}_y^\top \Sigma_y^{-1} \tilde{Z}_y + n_y \log(2\pi) \right).$$

where n_y is the number of observations used in year y . This likelihood treats data from different years as independent. To maximize the likelihood in terms of the parameters, we use the optimization L-BFGS-B algorithm due to [Byrd et al. \(1995\)](#) implemented in the `optim` function in R.

An obstacle for the maximization is the use of real-time salinity data, which are not fully quality controlled and cannot be left out of the definition of $\tilde{Z}_{i,\cdot}$ and $\tilde{W}_{i,\cdot}$. Using this data can affect the model parameters and resulting predictions. To overcome this issue, we use a standard approach with an expectation-maximization-type (EM) algorithm:

1. (E step) Using the temperature, delayed-mode salinity data, and the estimated parameters, form a prediction for the real-time salinity scores. In the first iteration, the prediction of the real-time salinity scores are 0.
2. (M step) Using all data as if it were delayed-mode, estimate the model parameters via maximum likelihood.
3. Return to the E step.

This treats the real-time salinity scores as unobserved, latent variables. At each grid point, 6 iterations of the algorithm are done, and the parameter estimates from the final M step are used. This choice strikes a balance between computation time and statistical accuracy; in examples, the differences between estimated parameters from consecutive steps decrease quickly after the first few steps. Estimating the joint dependence between temperature and salinity is not considered in [Kuusela and Stein \(2018\)](#) and [Roemmich and Gilson \(2009\)](#). While it requires additional computation, it provides a more comprehensive analysis of the Argo data and enables us to predict functionals of temperature and salinity such as potential density and potential temperature that take into account their dependence. The estimated parameters can be viewed using an R Shiny application in [Appendix A.2](#).

4.3. *Estimation of the measurement error variance $\kappa(p)$.* In (7), we have outlined a model involving the additional variance term $\epsilon_{i,j}$ as independent error with some variance $\kappa(p)$. To give full uncertainties for our predictions, we estimate $\kappa(p)$ as follows. At each location, a smoothing spline is fit with the observations

$$R_{i,j} = \log \left(\left(Y_{i,j}^0 - \sum_{k=1}^{K_1} Z_{i,k} \phi_k(p_{i,j}) \right)^2 \right)$$

by solving the minimization problem

$$\frac{1}{n} \sum_{i=1}^n \frac{K_{h_s, h_t}(s_i - s_0, d_i - d_0)}{m_i} \sum_{j=1}^{m_i} (R_{i,j} - \beta(p_{i,j}))^2 + \lambda \left\| \beta^{(2)} \right\|_{\mathbb{L}_2}^2,$$

an approach similar to the mean estimation in [Section 3](#) with cross validation. The logarithm ensures that the variances are nonnegative, and the transformed estimate $\hat{\kappa}(p) =$

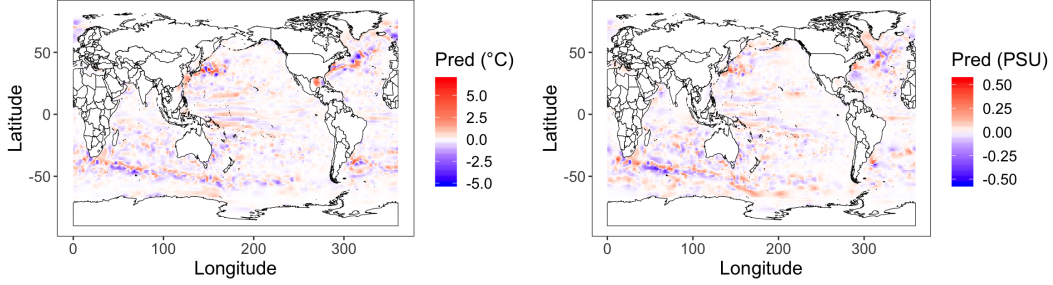


FIG 7. February 2012 predictions for temperature (**Left**) and salinity (**Right**) residuals, 300 dbar.

$2 \cdot \exp(\beta(p) + \varphi(1))$, where $\varphi(x)$ is the digamma function, gives a bias-corrected estimate of the remaining variance not captured in the modeling of the first K_1 scores. We compute this for temperature and salinity separately.

4.4. Predictions, Uncertainties, and Prediction Bands. In this section, we employ the estimated covariance for functional spatial kriging that takes into account dependence in depth. Under the assumptions of our model, this provides an optimal functional prediction at an unobserved location. To detail this approach, let Σ_y be estimated covariance matrix of the decorrelated scores $\tilde{Z}_{y_*} = (\tilde{Z}_{i,k})_{i=1}^{n_{y_*}}$ for a fixed k in an area around a fixed location for a year y_* . The conditional distribution of $\tilde{Z}_{*,k} := \tilde{Z}_k(s_*, d_*, y_*)$ at an unobserved location is

$$\tilde{Z}_{*,k} | Y^0 \sim N \left(\Sigma_{12}^\top \Sigma_{y_*}^{-1} \tilde{Z}_{y_*}, \gamma_k + \sigma_k^2 - \Sigma_{12}^\top \Sigma_{y_*}^{-1} \Sigma_{12} \right)$$

where $\Sigma_{12} = \text{Cov} \left(\tilde{Z}_{*,k}, \tilde{Z}_{y_*} \right)$. We similarly obtain the predictions for the decorrelated salinity scores $\tilde{W}_{*,k}$. From these estimated distributions of the $\tilde{Z}_{*,k}$ and $\tilde{W}_{*,k}$, using the relation that $\begin{pmatrix} Z_* \\ W_* \end{pmatrix} = V \begin{pmatrix} \tilde{Z}_* \\ \tilde{W}_* \end{pmatrix}$ described in (16), the conditional distribution of the original scores is

$$\begin{pmatrix} Z_* \\ W_* \end{pmatrix} | Y^0 = V \begin{pmatrix} \tilde{Z}_* \\ \tilde{W}_* \end{pmatrix} | Y^0 \sim N \left(V \mathbb{E} \left\{ \begin{pmatrix} \tilde{Z}_* \\ \tilde{W}_* \end{pmatrix} | Y^0 \right\}, V \text{Var} \left\{ \begin{pmatrix} \tilde{Z}_* \\ \tilde{W}_* \end{pmatrix} | Y^0 \right\} V^\top \right).$$

The conditional distribution of $T^0(s, d, y, p)$ and $S^0(s, d, y, p)$ can be found using (18) or (12) and (13), providing a prediction for any pressure. In Figure 7, we give the predictions for a fixed pressures of 300 dbar on the 1 degree by 1 degree grid.

We test the uncertainty estimates based on this model in a leave-one-profile-out manner. For each February profile, the profile is left out, and nearby profiles are used to predict at the location and time of the profile. Then, the left-out profile is compared with the predictions. For salinity, only delayed-mode profiles are compared. For each quantity, we use bounds of two standard deviations from the mean, which corresponds to approximately a 95.4 percent prediction interval. For brevity, we develop uncertainties for temperature, and similar bounds are obtained for salinity. We consider both pointwise and uniform prediction bounds on the residual curves $Y_{i,j}^0 = \phi(p_{i,j})^\top Z_{*,\cdot} + \epsilon_{i,j}$. The pointwise $1 - \alpha$ interval for the

TABLE 1
Average pointwise coverages of intervals and bands over all pressures

Quantity	# Profiles	Pointwise Coverage	Band Coverage
Temperature	76,016	96.9	96.1
Salinity	45,188	97.8	95.9
Nominal level		95.4	95.4

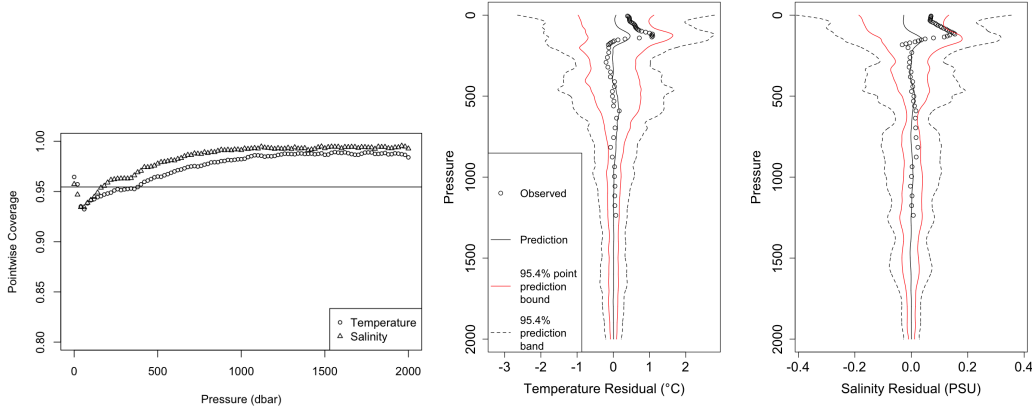


FIG 8. Average pointwise coverage of 95.4% confidence intervals summarized in 20 dbar increments for temperature and salinity (**Left**). The horizontal line indicates the nominal level. The intervals reach coverage for most pressures. Example of cross validation for (**Middle**) temperature and (**Right**) salinity. The shown profile is float 1901400, cycle 41, observed in the Southwest Indian Ocean (40.6 degrees East, 39.5 degrees South, 2011). A functional prediction over all pressure is provided, and the intervals capture the increased variability near the ocean surface. The simultaneous band gives considerably larger width than the pointwise bound.

residual at pressure $p_{i,j}$, based on (12) and (13), is

$$\phi(p_{i,j})^\top \mathbb{E} \{Z_{*,\cdot} | Y^0\} \pm q_{1-\alpha/2} \sqrt{\phi(p_{i,j})^\top \text{Var} \{Z_{*,\cdot} | Y^0\} \phi(p_{i,j}) + \hat{\kappa}(p_{i,j})}.$$

where $q_{1-\alpha/2}$ is the $1 - \alpha/2$ quantile of $N(0, 1)$. In addition, we develop simultaneous predictions bands over pressure by using the approach of Choi and Reimherr (2018) reviewed in Appendix A.6.

In our empirical coverages in Table 1 (where $K_1 = K_2 = 10$), the intervals and bands show good coverage for both temperature and salinity. In Table 1, the band coverage refers to the proportion of profiles for which every observation of the profile that was left out was covered by the estimated band. The pointwise coverages correspond to the proportion of all measurements covered by the intervals over all pressures. When summarizing the pointwise coverages by pressure in Figure 8, the coverage is achieved for most of the pressure dimension, though typically the intervals in the range 20-200 dbar do not meet full coverage. The conservatism of the uncertainty estimates for deeper pressures may be due to a lack of empirical independence between $Z_k(s, d, y)$ and $\epsilon_{i,j}$. In Figure 8, we show the functional prediction, interval, and band for one profile.

4.5. *Validation and comparison.* We compare our approach with the reference model and Model 5 of Kuusela and Stein (2018), which we refer to as the Roemmich and Gilson-type reference model and KS in this subsection, with respect to predictions at fixed levels. In Appendix A.8, we compare the differences between the KS and functional predictions at 10, 300, and 1500 dbar and find them to be generally comparable. Also, we can compare the predictive errors through the cross validation approach described in the previous subsection. Our functional approach enables the prediction of temperature and salinity *without* interpolation onto fixed pressure levels. To provide a comparison with the fixed pressure levels of KS, we compute summaries of the residuals by breaking up the interval $[0, 2000]$ using the midpoints of the Roemmich and Gilson pressure levels. For example, the interval $(6.25, 15]$ corresponds to the Roemmich and Gilson pressure level 10 dbar, $(290, 310]$ corresponds to 300 dbar, and $(1456.25, 1550]$ corresponds to 1500 dbar. Not all profiles are included in the comparison. For KS, profiles are removed in boundary seas and where the interpolation fails, that is, where there are no measurements either above or below the relevant pressure level, and we remove them in this comparison as well and only use profiles included in KS at any of 10, 300, and 1500 dbar. The prediction errors are evaluated by the root mean squared error (RSME) defined as $\sqrt{\frac{1}{n} \sum_{i=1}^n (y_{i,p} - \hat{y}_{i,p})^2}$ and the 50% (median) and 75% (3rd quartile) quantiles of $|y_{i,p} - \hat{y}_{i,p}|$ where $y_{i,p}$ are the measurements corresponding to pressure level p , and $\hat{y}_{i,p}$ are the predictions for that measurement.

We show the results in Table 2 and Figure 9 and comment on them. Our method clearly outperforms the Roemmich and Gilson-type reference model and has approximately the same the prediction error as KS. Notably, we suspect that avoiding interpolation onto pressure levels considerably improves our prediction error, especially at greater depths. For example, at 1500 dbar, the RMSE for the functional model outperforms KS, though it trails in the outlier-resistant measures of the median and 3rd quartile. This is due to a small number profiles that have sparse measurements at greater depths, leading to poor quality of interpolation in pressure. This generally holds true at the other levels, with the RSME being more favorable compared to the median and 3rd quartile for the functional approach. At 300 decibars, our functional model improves upon KS for each of the metrics, and at 10 decibars, the functional model is slightly worse. We explain a possible reason for this gap at 10 decibars. When ignoring the yearly variation in the mean, the correlation lengths in space decrease drastically when moving from 10-20 dbar to 40-50 dbar in some locations. This persists to a lesser extent when the yearly variation is modeled. Due to this effect, a pointwise approach as in KS can better model the surface pressure levels because the conditions in the small width of the interval near the surface are not easily isolated by the scores. This motivates future work on a new space-time functional model that allows a scale parameter to change smoothly but quickly as a function of pressure (ref. Section 6). Our functional approach reduces the variability of the residuals over all pressures for both temperature and salinity. The reduction in RMSE from the mean to the prediction is larger for temperature, possibly due to only using delayed-mode data for salinity.

In Appendix A.4, the computational costs of our approach and KS are roughly compared. We conclude that, when focusing on temperature, the FDA approach can provide similar predictions for all pressures in roughly the same amount of time it takes to compute a pointwise approach for 13 pressure levels. Thus, our approach can provide approximately a

TABLE 2
Comparison of KS and Functional Approach prediction errors, temperature

Pressure	Metric	RG residuals	Functional residuals	RG-type model	KS	Functional model
10	RMSE	0.8889	0.7540	0.6135	0.5072	0.5223
10	Q3	0.8670	0.6247	0.5026	0.3735	0.3972
10	Median	0.4750	0.3193	0.2556	0.1801	0.1978
300	RMSE	0.8149	0.8552	0.5782	0.5124	0.4980
300	Q3	0.6320	0.6845	0.4213	0.3684	0.3666
300	Median	0.3062	0.3494	0.1991	0.1740	0.1727
1500	RMSE	0.1337	0.1381	0.1014	0.0883	0.0826
1500	Q3	0.1043	0.1160	0.0736	0.0641	0.0724
1500	Median	0.0530	0.0620	0.0356	0.0311	0.0376

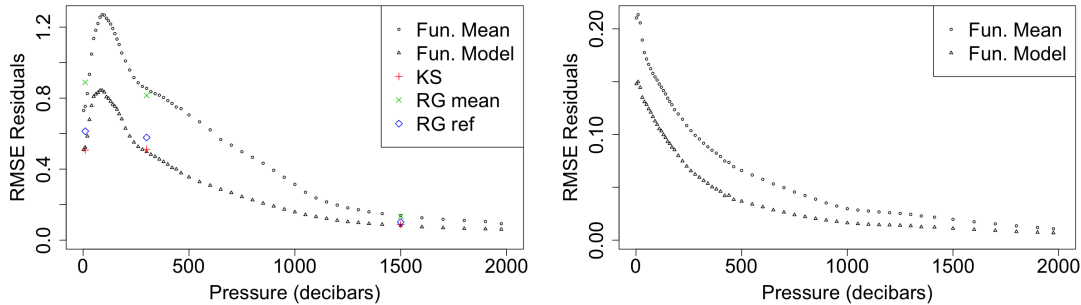


FIG 9. Comparison of RMSE by RG pressure level for temperature (*Left*) and salinity (*Right*). The KS, RG mean, and RG ref numbers are included from [Kuusela and Stein \(2018\)](#), where KS refers to the space-time Gaussian model, the RG mean refers to the Roemmich and Gilson mean, and RG ref refers to the implemented Roemmich and Gilson-like covariance. The variability is largest for salinity near the surface, while for temperature the largest variability lies near the typical thermocline area below the surface. The functional mean results in less variable residuals near the surface compared to the RG mean because yearly effects are included in the functional mean.

4 to 5 times speedup when considering the 58 Roemmich and Gilson pressure levels.

5. Applications: Ocean Heat Content and Mixed Layer Depth. The procedures of Sections 3 and 4 result in estimated functions of temperature and salinity at each location. For these functions, derivatives and integrals can be easily calculated. Also, other oceanographic measures of interest, like potential density, can be derived directly from the estimated temperature and salinity from TEOS-10 in R ([Kelley, Richards and WG127 SCOR/IAPSO, 2017](#)). In this section and Appendix A.10 and A.11, we present a general framework for leveraging these estimates for other scientific problems and give two examples in ocean heat content and estimating the mixed layer depth.

5.1. *Ocean Heat Content.* The amount of heat contained in the ocean is of great interest for global climate change and has been studied extensively, since the ocean absorbs the majority of the Earth’s excess heat. A non-exhaustive list includes [Levitus et al. \(2012\)](#), [Roemmich et al. \(2015\)](#), [Lyman and Johnson \(2013\)](#), [Roemmich, Gould and Gilson \(2012\)](#),

and [Johnson and Birnbaum \(2017\)](#).

While integrating temperature over pressure describes the amount of heat in the ocean, it is biased since the temperature of two volumes of water with the same amount of heat content at two different pressures is different. For this reason, conservative temperature is more commonly used for heat content estimates ([McDougall, 2003](#)). Conservative temperature can be calculated using the standard oceanographic toolbox [McDougall and Barker \(2011\)](#) which is implemented in R from [Kelley, Richards and WG127 SCOR/IAPSO \(2017\)](#). We use the Delta method approach in [Section A.10](#) to estimate its distribution. Denote conservative temperature as a function of temperature, practical salinity, and pressure at a location as $\Theta(t, s, p)$ and the ocean heat content at a location as

$$Q = \int_0^{p^*} c_p \rho \Theta(T(p), S(p), p) dp$$

where c_p and ρ are constants (the specific heat capacity and density of seawater, respectively). We apply the Delta method as described in [Section A.12](#).

Anomalies from the mean are computed for each year as $\mathbb{E}\{Q|Y^0\} - \mathbb{E}\{Q\}$, where $\mathbb{E}\{Q\}$ is the ocean heat content given by year-averaged mean $\bar{\beta}(p) = \frac{1}{10} \sum_{y=2007}^{2016} \beta_{0,y}(p)$, and an example of these estimates and standard deviations are shown in [Figure 10](#) for February 2016. We compare the estimates for 0-700 dbar with the estimates available at [NOAA NODC \(2019\)](#) that employ the [Levitus et al. \(2012\)](#) approach to estimation of ocean heat content. The large-scale features of the fields are similar, though our integrated functions show finer-detail and smaller-scale features as well. Our field is an estimate for a specific time point of mid-February, while the estimates available from NOAA are a January-to-March average, which we hypothesize explains much of the difference in smoothness and features shown in the fields. There are two main regions in the Pacific Ocean where the heat content is significantly above or below its year-averaged mean value based on our uncertainty estimates. One can view similar plots for other years using the R Shiny application available in the [Section A.2](#). The FDA approach, by modeling the dependence between different pressures, makes these uncertainty estimates possible between any two pressures in $[0, 2000]$ as a natural consequence of our functional kriging approach.

5.2. Estimation of Mixed Layer Depth. Having complete functional predictions gives valuable information on the shape of the curve, which we apply to estimate the depth of the mixed layer. The mixed layer is a section of the ocean near the surface where the water mixes freely, giving near uniform properties of temperature, salinity, and density. The mixed layer governs the interaction between the atmosphere and the ocean, and thus its study can reveal information about the carbon uptake and heat content of the ocean, among others features ([Holte et al., 2017](#)). During the summer, the temperature at the surface will rise considerably, and the mixed layer is shallower. During the winter, the mixed layer deepens to a lower temperature, resulting in large seasonal changes of its depth. However, the year-to-year variability in mixed layer depth is not as well understood. Our goal is to find an estimate of mixed layer depth (MLD). Most approaches for MLD estimation use the temperature or potential density profiles. See [Sections 4.2 and 7.4 of Talley et al. \(2011\)](#) and [Holte and Talley \(2009\)](#) for details on estimating mixed layer depth. Two common approaches for estimating the mixed layer are threshold and derivative algorithms. The threshold algorithm is defined

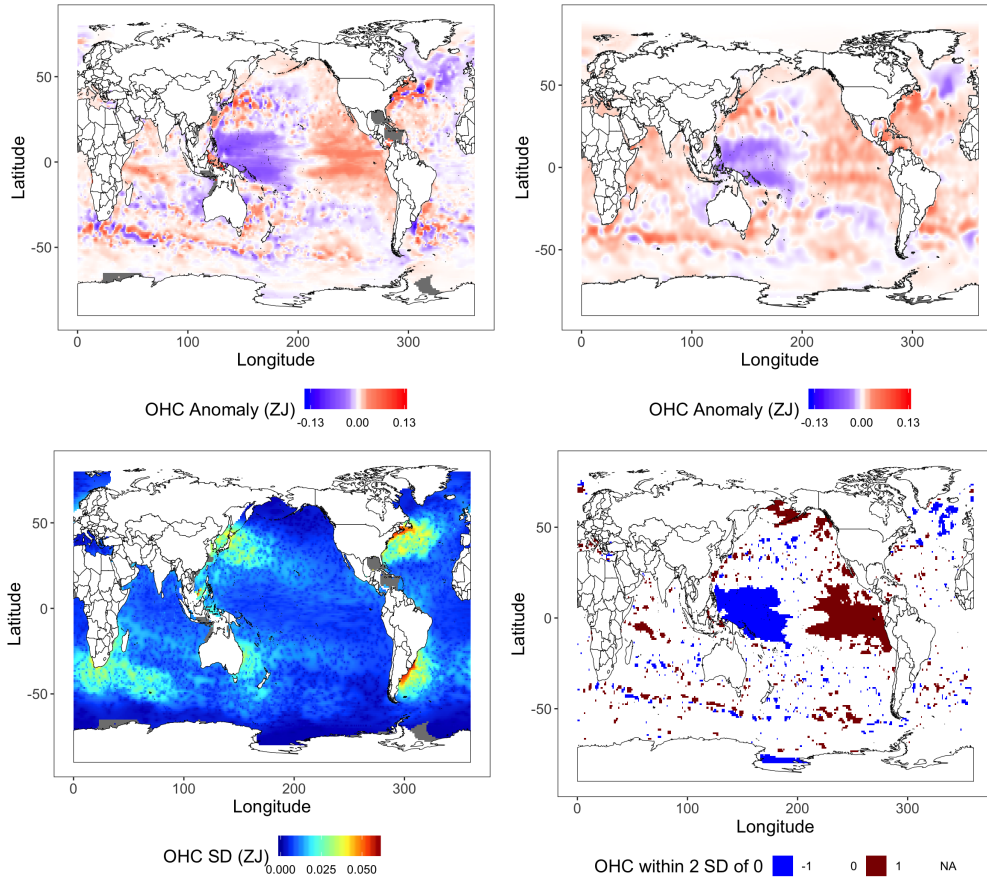


FIG 10. (*Top Left*) Ocean heat content anomaly estimates from the year-averaged mean, February 2016 functional estimate integrated for 0-700 dbar, (*Top Right*) NOAA estimate for 0-700 m, January-March 2016 average. (*Bottom Left*) our estimates of the standard deviation of OHC at each location and (*Bottom Right*) whether the OHC anomaly was within 2 standard deviations of 0 where red (blue) is above (below) 2 standard deviations.

as the smallest depth for which the temperature or density changes a certain amount from its surface value, and the derivative algorithm is defined by the smallest depth for which the derivative of the response reaches a threshold. Both algorithms are easily implemented using our functional predictions of temperature and salinity.

The uncertainty in the resulting estimates is assessed using the parametric bootstrap approach described in Section A.10, which works better than a Delta method approach, though it is more computationally intensive. For each location and year, we simulate $B = 1000$ times. We present results using the variable density threshold approach described in Holte et al. (2017), where the mixed layer depth is chosen as the first depth for which potential density decreases an amount corresponding to a temperature decrease of 0.2°C . In addition, we compute threshold and derivative estimates of the mixed layer depth. For temperature, we use a threshold of 0.2°C and a derivative value of $-0.025^\circ\text{C}/\text{dbar}$. For density, we use a threshold of $0.03 \frac{\text{kg}}{\text{m}^3}$ and a derivative value of $-0.025 \frac{\text{kg}}{\text{m}^3 \cdot \text{dbar}}$. Choices for these values are the same or close to those reviewed in Holte and Talley (2009).

For the variable potential density threshold approach, the results are shown in Figure 11. The difference between the median and mean plots suggest that the MLD for some areas near Greenland and the Labrador sea have skewed distributions. Comparing the top left (average over all years) and bottom left (average for 2014), the summaries for a single year are generally rougher than the average over years, and the estimates for 2014 show deviations from the average MLD. In addition to basic summary statistics, our approach provides arbitrary quantiles of mixed layer depth, as shown with the 80th percentile. In Figure 12, we compare the results with the mean density threshold climatology of mixed layer depths from Holte et al. (2017) available at <http://mixedlayer.ucsd.edu/>. For the climatology of Holte et al. (2017), mixed layer depths are calculated for individual profiles, which are then averaged on a grid in space. The functional mixed layer depths are somewhat shallower than those in Holte et al. (2017) in some areas. Similar plots for other years are available using the R Shiny application in the Appendix A.2.

In addition to providing estimates, we give simulation-based uncertainties in Figure 12. The uncertainty estimates are generally much higher where there is a deeper mixed layer. This is partially a reflection that the temperature quickly decreases from shallow, summer mixed layers, while for deep, winter mixed layers, the transition between the mixed layer and below is less steep and thus harder to detect or define. The FDA estimates of mixed layer provide comprehensive estimates of mixed layer depth by providing an entire predictive distribution of MLD at each location and for each year. Our estimates could be incorporated into a more complex algorithm for the mixed layer depth that combines multiple estimates of the mixed layer depth similar to Holte and Talley (2009).

6. Conclusion and Future Directions. The Argo data is an exemplary modern dataset that motivates new statistical approaches, development of methodology, and appropriate statistical applications. In this paper, we have provided the first comprehensive functional-data analysis of the Argo data which addresses methodological and computational challenges for mean estimation, covariance estimation, functional kriging, and estimation of functionals of the estimates. Our approach avoids the simplification of data in pressure via interpolation which limits other methods' ability to provide a comprehensive analysis. The predicted functions give powerful new tools to fully explore important scientific problems. Furthermore, our approach can decrease the computational burden of prediction by sharing information across pressure. Our estimates match well or outperform existing methodologies that estimate ocean properties at fixed pressure levels. Our analysis also introduces the local estimation of functional estimates and represents a leap forward in the analysis of spatio-temporal functional data. For example, our mean estimation approach establishes a new, computationally-efficient, hybrid methodology that combines kernel estimation and smoothing splines.

Throughout our approach, there are areas for improvement. For mean estimation for Stage 1, one would want to select the amount of nearby data adaptively and allow for elliptical regions in space. This is especially important for areas in the Western boundary currents and other areas where changes in ocean properties are highly directional in space. One approach would be to extend algorithms from local regression that choose the bandwidth to this functional model. Using iteratively reweighted least squares or more careful smoothing parameter selection may also give improvements.

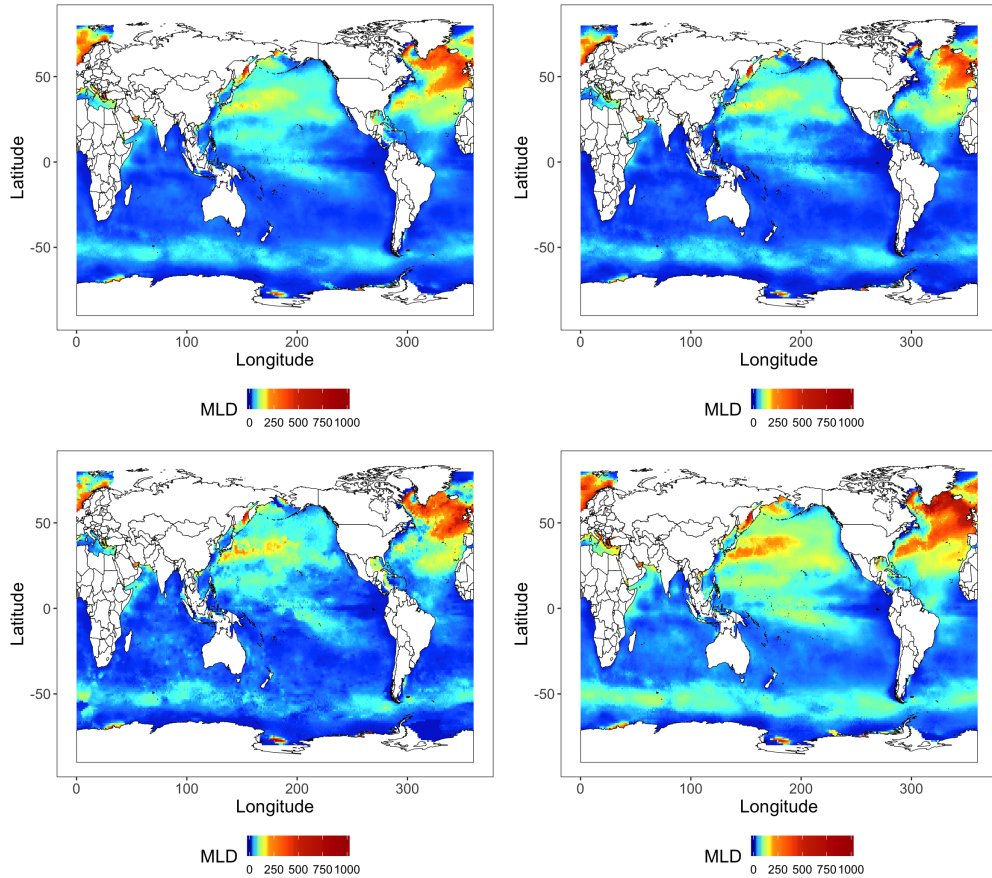


FIG 11. February mixed layer depth in dbar by the variable threshold approach (**Top Left**) averaged over all years, (**Top Right**) average of median of each year, (**Bottom Left**) mean of 2014, (**Bottom Right**) average of 80th percentile of each year. The algorithm picks out both shallow mixed layers in the summer in the Southern Hemisphere as well as deeper mixed layers in the winter for the Northern Hemisphere. The average and quantiles greater than .5 tend to pick out deeper mixed layers in the Northern Atlantic and Labrador sea that match closer to other mixed layer depth estimates.

For our spatial covariance modeling for Stage 2, we employ a relatively simple model that successfully captures key features by jointly modeling temperature and salinity. In general, we are limited by computational challenges, which could be addressed with approximate models, e.g., Vecchia’s approximation (Guinness, 2019) or the SPDE approach (Lindgren, Rue and Lindström, 2011). More complexity should be explored in the models. For example, a functional model that allows rapid changes in the scale parameter as a function of depth would likely improve upon our model. In addition, there is some evidence that the cross-covariance between vectors of principal component scores include non-reversible, i.e. asymmetric, dependence, which is not available in the scalar Matérn-type multivariate models. In addition, one could explore non-Gaussian models, which could provide better coverage for prediction intervals as demonstrated in Kuusela and Stein (2018) and Bolin and Wallin (2019). Also, we have only modeled the local spatial dependence, and ideally, one would also like to combine estimates across space with uncertainty, for example, using

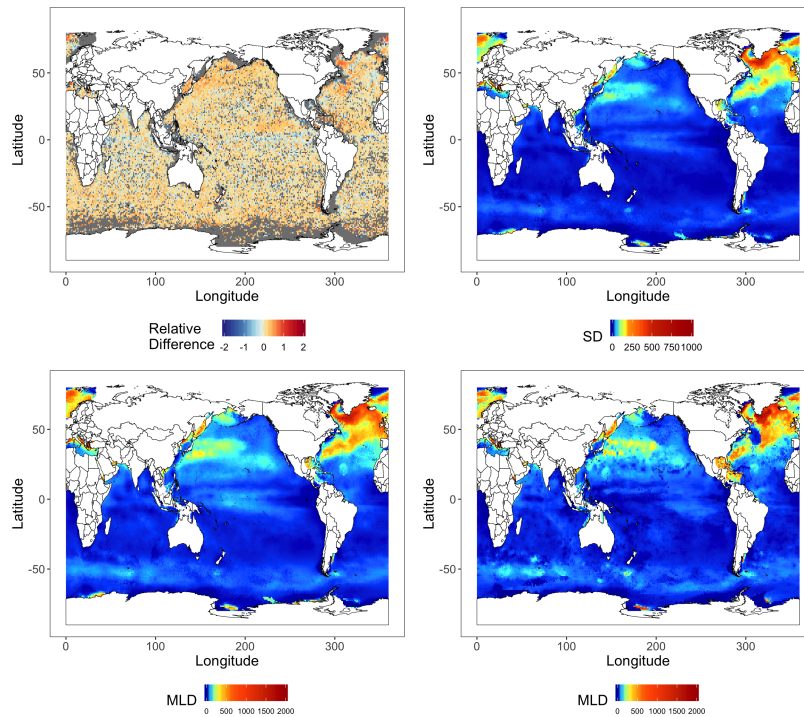


FIG 12. February mixed layer depth (**Top Left**) relative difference of mean functional approach and *Holte et al. (2017)* threshold method (i.e. $(HT - FUN)/HT$), (**Top Right**) mean of standard deviation estimates (dbar), (**Bottom Left**) average length of 5% to 95% range (dbar), (**Bottom Right**) 2014 length of 5% to 95% range (dbar). The functional estimates are shallower than *Holte et al. (2017)* near Japan and the Labrador Sea and slightly deeper in the Indian Ocean, and otherwise are similar. Our functional approach suggests the largest variability in the North Atlantic.

an approach similar to *Wiens, Nychka and Kleiber (2020)*. This would enable uncertainty estimates for global ocean heat content.

There is a wide variety of statistical research directions using the Argo data, many of which are noted in the conclusion of *Kuusela and Stein (2018)*. For instance, one would want to consider additional biogeochemical variables that a limited set of Argo floats measure as well as explore the sampling scheme of Argo profiles as they drift in the ocean that is nonstandard in spatial statistics. Although we have considered many standard approaches in FDA for use on the Argo data, there are more tools that could be applied, including clustering of profiles, functional regression, canonical correlation analysis, hypothesis testing, and data fusion with scalar data like sea surface temperature obtained from satellite measurements. Moreover, the Argo data calls for full methodological and theoretical development of the field of space-time functional data, for which potential research problems could be developed. For example, the large-sample properties of the methodology used in this paper could be explored under functional and spatial dependence.

References.

- ARGO (2000). Argo float data and metadata from Global Data Assembly Centre (Argo GDAC). *SEANOE*.
- BOLIN, D. and WALLIN, J. (2019). Multivariate type G Matrn stochastic partial differential equation random fields. *Journal of the Royal Statistical Society: Series B (Statistical Methodology)* **82** 215-239.
- BYRD, R., LU, P., NOCEDAL, J. and ZHU, C. (1995). A limited memory algorithm for bound constrained optimization. *SIAM Journal of Scientific Computing* **16** 1190-1208.
- CHANG, W., CHENG, J., ALLAIRE, J., XIE, Y. and MCPHERSON, J. (2018). shiny: Web Application Framework for R R package version 1.2.0.
- CHOI, H. and REIMHERR, M. (2018). A geometric approach to confidence regions and bands for functional parameters. *Journal of the Royal Statistical Society: Series B (Statistical Methodology)* **80** 239-260.
- DAVIS, T. A. (2006). sparseinv: Sparse Inverse Subset. SIAM Direct Methods for Sparse Linear Systems.
- DELICADO, P., GIRALDO, R., CARLOS, C. and MATEU, J. (2010). Statistics for spatial functional data: some recent contributions. *Environmetrics: The official journal of the International Environmetrics Society* **21** 224-239.
- ERISMAN, A. M. and TINNEY, W. F. (1983). On computing the inverse of a sparse matrix. *Communications of the ACM* **18** 177-179.
- FAN, J. and GIJBELS, I. (1996). *Local Polynomial Modelling and its Applications. Monographs on Statistics and Applied Probability* **66**. Chapman & Hall, London. [MR1383587](#)
- GREEN, P. J. and SILVERMAN, B. B. (1994). *Nonparametric Regression and Generalized Linear Models*. Springer-Science+Business Media, B.V.
- GUINNESS, J. (2019). Gaussian process learning via fisher scoring of Vecchia's approximation. arXiv: 1905.08374.
- HALL, P., MÜLLER, H.-G. and WANG, J.-L. (2006). Properties of principal component methods for functional and longitudinal data analysis. *The Annals of Statistics* **34** 1493-1517. arXiv: math/0608022.
- HOLTE, J. and TALLEY, L. (2009). A new algorithm for finding mixed layer depths with applications to Argo Data and subantarctic mode water formation. *Journal of Atmospheric and Oceanic Technology* **26** 1920-1939.
- HOLTE, J., TALLEY, L. D., GILSON, J. and ROEMMICH, D. (2017). An Argo mixed layer climatology and database. *Geophysical Research Letters* **44** 5618-5626.
- HSING, T. and EUBANK, R. (2015). *Theoretical Foundations of Functional Data Analysis with an Introduction to Linear Operators*. Wiley.
- HUTCHINSON, M. F. and DE HOOG, F. R. (1985). Smoothing noisy data with spline functions. *Numerische Mathematik* **47** 99-106.
- JOHNSON, G. C. and BIRNBAUM, A. N. (2017). As El Nio builds, Pacific Warm Pool expands, ocean gains more heat. *Geophysical Research Letters* **44** 438-445.
- KELLEY, D., RICHARDS, C. and WG127 SCOR/IAPSO (2017). gsw: Gibbs Sea Water Functions R package version 1.0-5.
- KING, M. C., STAICU, A.-M., DAVIS, J. M., REICH, B. J. and EDER, B. (2018). A functional data analysis of spatiotemporal trends and variation in fine particulate matter. *Atmospheric Environment* **184** 233-243.
- KOKOSZKA, P. and REIMHERR, M. (2019). Some recent developments in inference for geostatistical functional data. *Revista Colombiana de Estadística* **42** 101-122.
- KUUSELA, M. and STEIN, M. L. (2018). Locally stationary spatio-temporal interpolation of Argo profiling float data. *Proceedings of the Royal Society A: Mathematical, Physical and Engineering Sciences* **474** 20180400.
- LEVITUS, S., ANTONOV, J. I., BOYER, T. P., BARANOVA, O. K., GARCIA, H. E., LOCARNINI, R. A., MISHONOV, A. V., REAGAN, J. R., SEIDOV, D., YAROSH, E. S. and ZWENG, M. M. (2012). World ocean heat content and thermosteric sea level change (02000 m), 1955-2010. *Geophysical Research Letters* **39** L10603.
- LI, Y. and HSING, T. (2010). Uniform convergence rates for nonparametric regression and principal component analysis in functional/longitudinal data. *The Annals of Statistics* **38** 3321-3351.
- LINDGREN, F., RUE, H. and LINDSTRÖM, J. (2011). An explicit link between Gaussian fields and Gaussian Markov random fields: the stochastic partial differential equation approach. *Journal of the Royal Statistical Society: Series B (Statistical Methodology)* **73** 423-498.
- LYMAN, J. M. and JOHNSON, G. C. (2013). Estimating global ocean heat content changes in the upper 1800 m since 1950 and the influence of climatology choice. *Journal of Climate* **27** 1945-1957.

- LYNCH, B. and CHEN, K. (2018). A test of weak separability for multi-way functional data, with application to brain connectivity studies. *Biometrika* 815831. arXiv: 1703.10210.
- MARTÍNEZ-HERNÁNDEZ, I. and GENTON, M. G. (2020). Recent developments in complex and spatially correlated functional data. arXiv: 2001.01166.
- MCDUGALL, T. J. (2003). Potential enthalpy: a conservative oceanic variable for evaluating heat content and heat fluxes. *Journal of Physical Oceanography* **33** 945-963.
- MCDUGALL, T. J. and BARKER, P. M. (2011). Getting started with TEOS-10 and the Gibbs Seawater (GSW) Oceanographic Toolbox. *SCOR/IAPSO WG127* **33** 28.
- MONESTIEZ, P. and NERINI, D. (2008). A cokriging method for spatial functional data with applications in oceanology. In *Functional and Operatorial Statistics* (S. DABO-NIANG and F. FERRATY, eds.). *Contributions to Statistics* 237-242. Physica-Verlag HD, Heidelberg.
- NOAA NODC (2019). Ocean Climate Laboratory, Global Ocean Heat and Salt Content Global Anomaly Fields. *National Oceanographic Data Center*.
- OWENS, W. B. and WONG, A. P. S. (2009). An improved calibration method for the drift of the conductivity sensor on autonomous CTD profiling floats by θ S climatology. *Deep Sea Research Part I: Oceanographic Research Papers* **56** 450-457.
- PAUTHENET, E., ROQUET, F., MADEC, G., SALLÉE, J.-B. and NERINI, D. (2019). The thermohaline modes of the global ocean. *Journal of Physical Oceanography* **49** 2535-2552.
- RAMSAY, J. and SILVERMAN, B. W. (2013). *Functional Data Analysis. Springer Series in Statistics*. Springer Science & Business Media, New York, NY.
- RAMSAY, J., WICKHAM, H., GRAVES, S. and HOOKER, G. (2018). fda: Functionral Data Analysis R package version 2.4.8.
- RODRÍGUEZ, A., DUNSON, D. B. and GELFAND, A. E. (2009). Bayesian nonparametric functional data analysis through density estimation. *Biometrika* **96** 149-162.
- ROEMMICH, D. and GILSON, J. (2009). The 2004-2008 mean and annual cycle of temperature, salinity, and steric height in the global ocean from the Argo Program. *Progress in Oceanography* **82** 81-100.
- ROEMMICH, D., GOULD, W. J. and GILSON, J. (2012). 135 years of global ocean warming between the Challenger expedition and the Argo Programme. *Nature Climate Change* **2** 425-428.
- ROEMMICH, D., CHURCH, J., GILSON, J., MONSELESAN, D., SUTTON, P. and WILFFELS, S. (2015). Unabated planetary warming and its ocean structure since 2006. *Nature Climate Change* **5** 240-245.
- STEIN, M. L. (2013). *Interpolation of Spatial Data: Some Theory for Kriging*. Springer, New York. OCLC: 968504419.
- TALLEY, L. D., PICKARD, G. L., EMERY, W. J. and SWIFT, J. H. (2011). *Descriptive Physical Oceanography (Sixth Edition)*, Sixth edition ed. Academic Press, Boston.
- TOWNS, J., COCKERILL, T., DAHAN, M., FOSTER, I., GAITHER, K., GRIMSHAW, A., HAZLEWOOD, V., LATHROP, S., LIFKA, D., PETERSON, G. D., ROSKIES, R., SCOTT, J. R. and WILKINS-DIEHR, N. (2014). XSEDE: Accelerating Scientific Discovery. *Computing in Science & Engineering* **16** 62-74.
- WAHBA, G. (1990). *Spline Models for Observational Data* **59**. Siam.
- WICKHAM, H. (2016). *ggplot2: Elegant Graphics for Data Analysis*. Springer-Verlag New York.
- WICKHAM, H., FRANÇOIS, R., HENRY, L. and MÜLLER, K. (2019). dplyr: A Grammar of Data Manipulation R package version 0.8.3.
- WIENS, A., NYCHKA, D. and KLEIBER, W. (2020). Modeling spatial data using local likelihood estimation and a Matérn to SAR translation. 1-20. arXiv: 2002.01124.
- WOOD, S. N. (2006). Low-rank scale-invariant tensor product smooths for generalized additive mixed models. *Biometrics* **62** 1025-1036.
- ZAMMIT-MANGION, A. (2018). sparseinv: Computation of the Sparse Inverse Subset R package version 0.1.3.
- ZHANG, H. and LI, Y. (2020). Unified principal component analysis for sparse and dense functional data under spatial dependency. *Under Review* 29.
- ZHANG, X. and WANG, J.-L. (2016). From sparse to dense functional data and beyond. *The Annals of Statistics* **44** 2281-2321.

APPENDIX A: NOTES, METHODOLOGICAL AND COMPUTATIONAL DETAILS

A.1. Acknowledgements. First, we thank the physical oceanography group at the Scripps Institution of Oceanography, including Sarah Gille, Lynne Talley, Matt Mazloff,

Isabella Rosso, John Gilson, and Dean Roemmich; in addition, we want to thank Mikael Kuusela, Alison Gray, and Donata Giglio.

These data were collected and made freely available by the International Argo Program and the national programs that contribute to it: <http://www.argo.ucsd.edu>. The Argo Program is part of the Global Ocean Observing System. This research was supported in part through computational resources and services provided by Advanced Research Computing at the University of Michigan, Ann Arbor. This work used the Extreme Science and Engineering Discovery Environment (XSEDE), which is supported by National Science Foundation grant number ACI-1548562 (Townes et al., 2014).

A.2. Code and Summary of R Shiny Applications. Code detailing each stage of analysis is available at <https://github.com/dyarger/argofda>. The Shiny Applications introduced in this paper are available with short descriptions at <https://sites.google.com/a/umich.edu/argostatistics/home/fdapaper>.

A.3. Details of Leverage Score Computation. In this subsection, we detail how one can take advantage of the local nature of the B-spline basis in computations while specifying a working correlation structure for the minimization problems of the type used in the mean estimation. This is a simple extension from past work, but this approach has not been considered for spline estimation before. Let $\{\chi_\ell\}_{\ell=1}^m$ be the B-spline basis used. Let Φ be the $(\sum_{i=1}^n m_i) \times M$ matrix, where $\sum_{i=1}^n m_i$ is the total number of observations and M is the number of basis functions, that gives the basis functions evaluated at each pressure. Specifically, the first row is given by $\{\chi_\ell(p_{1,1})\}_{\ell=1}^M$, and subsequent rows are evaluations for different $p_{i,j}$. Letting Σ^{-1} be the block diagonal matrix of $\frac{1}{nm_i} K_{h_s, h_t}(s_i - s_0, d_i - d_0) \Sigma_i^{-1}$, where Σ_i is the working covariance matrix such that Σ_i^{-1} is tridiagonal. Furthermore, let Ω be the penalty matrix of $\int_0^{2000} \chi_i^{(2)}(p) \chi_j^{(2)}(p) dp$ where $\{\chi_k\}_{k=1}^M$ is the B-spline basis used. Then the coefficients for the solution to (5) are $(\Phi^\top \Sigma^{-1} \Phi + \lambda \Omega)^{-1} \Phi^\top \Sigma^{-1} Y$. The leverage scores are defined as the diagonal elements of the matrix

$$A(\lambda) = \Phi(\Phi^\top \Sigma^{-1} \Phi + \lambda \Omega)^{-1} \Phi^\top \Sigma^{-1} \in \mathbb{R}^{n \times n}.$$

Let $B = \Phi^\top \Sigma^{-1} \Phi + \lambda \Omega$ and note that if Σ^{-1} is diagonal, B is also banded due to the sparsity pattern of Φ and Ω . Thus, one does not need to invert the entire matrix B , and since Φ is sparse, the diagonal of $A(\lambda)$ only relies on certain elements of B^{-1} . In this case, (Hutchinson and de Hoog (1985)) give an algorithm to compute the leverage scores.

Using a non-diagonal matrix Σ^{-1} means that B will no longer be banded, but may have additional non-zero entries depending on the basis used and the amount of separation between measurements in the same profile. Thus, the approach in Hutchinson and de Hoog (1985) no longer applies. However, for a more general sparse matrix, one can compute the leverage scores as given in Erisman and Tinney (1983). We detail the algorithm below. First, we obtain the Cholesky decomposition of $B = U^\top D U$, where U is upper triangular with unit diagonal entries, and D is diagonal. The Takahashi equation for the inverse is given by

$$(19) \quad B^{-1} = D^{-1} U^{-\top} + (I - U) B^{-1},$$

where we use the shorthand of notation $U^{-\top}$ to signify the transpose of U^{-1} .

One can simplify the computation of leverage scores as follows. Since B^{-1} is symmetric, one only needs to compute the upper triangular part of B^{-1} . Thus, since $U^{-\top}$ is lower triangular, we need only compute the diagonal entries of $D^{-1}U^{-\top}$, or, equivalently, the diagonal entries of D^{-1} . For a sparse matrix $I - U$, the relation (19) gives a recurrence relation for certain elements of B^{-1} . Each of these elements can be computed using elements previously computed below and to the right of the element. [Erisman and Tinney \(1983\)](#) describe the relation in Theorem 1: One can compute $(B^{-1})_{ij}$ for all i and j such that $U_{ij} \neq 0$ using U , D , and the values of $(B^{-1})_{kl}$ such that $U_{kl} \neq 0$ and $k > i$, $l > j$. That is,

$$(B^{-1})_{ij} = \frac{1}{d_{ii}}\delta_{ij} - \sum_{k=i+1}^p U_{ik}(B^{-1})_{kj}$$

where δ_{ij} is the Kronecker delta function. Thus, one can fill in certain elements of B^{-1} beginning in the bottom right and working one's way up the matrix.

In our context, these elements of B^{-1} are a superset of those needed for computing the diagonal of $A(\lambda) = \Phi B^{-1} \Phi^{\top} \Sigma^{-1}$. Furthermore, we need only the trace of $A(\lambda)$, so we compute $\text{tr}(\Phi B^{-1} \Phi^{\top} \Sigma^{-1}) = \text{tr}(B^{-1} \Phi^{\top} \Sigma^{-1} \Phi)$ using the circulant property of the trace and only using the elements of B^{-1} computed. We have the correct entries to compute because B is as or less sparse compared to $\Phi^{\top} \Sigma^{-1} \Phi$.

It is not clear how to include a correlation structure in the estimation of the covariance operator while maintaining the sparse structure of B , and including a correlation structure could improve the estimates of the principal component functions.

A.4. Computational Details. In Table 3, we give the computational run times and information on each of the stages of our analysis. We have developed efficient code for the B-spline evaluation matrices with speed and flexibility that are not currently available in R. These functions are based on the `smooth.spline` function that quickly computes a univariate spline and cannot include covariates. This function is functionally identical to the `eval.basis` function from the `fda` package for B-splines, but has better speed. Of each of the stages, the maximum likelihood estimation has the largest computational cost since it must be numerically maximized. Furthermore, it must be optimized for 20 scores, for six separate EM iterations. After the first iteration, we start the optimization at previous iteration parameters to speed things up and find that each successive EM iteration takes slightly less time. However, if one were to consider 10 scores for temperature, this would speed up the computations by more than half since the EM algorithm is not necessary. A smaller radius would also decrease the computation time, since this would reduce the size of the dense covariance matrices, for which computing the Cholesky decomposition is the largest computational cost in computing the likelihood. However, note that once the parameters are estimated, one can quickly predict as demonstrated by the cross validation column.

For the marginal covariance estimation, we reduced the number of observations used for each profile so that the number of cross products did not become too large. Without reducing the number of observations used for each profile, the median number of observations would be in the tens of millions, which is not realistic for computation with respect to both memory

and time. Although sparse matrices lessen the challenge, even forming the basis evaluation matrices can be prohibitive.

Based on the computational overview, multiplying the mean running time by the number of grid points, the sections represented takes approximately 7,100 core-hours to compute. However, given a new year of data, one can use the previously-estimated mean and covariance parameters at each grid point in approximately 50 core-hours, a tiny fraction of the overall total. For the computation, we use Michigan’s ARC-TS resources for these computations and to host the Shiny Applications. Also, some computations were run using XSEDE Bridges cluster.

TABLE 3

Overview of computations. We give the number of grid points for each step and the median number of running time, profiles, observations, cross validation evaluations, and the approximate computational complexity. Note that the number of observations for the marginal covariance estimation refers to the number of cross products used. Here, $N = \sum_{i=1}^n m_i$, $N_2 = \sum_{i=1}^n m_i^2$, $\tilde{n}_y = \max_y n_y$, and approximate computational complexity refers to the naive complexity with fixed bandwidth for each stage.

Metric	Mean (T)	Mean (S)	Marginal Cov (T)	Marginal Cov (S)	ML 20 scores (6 EM iter)	Nugget	Cross Validation
# Grid Points	47,938	46,023	41,775	41,132	41,124	41,025	76,016
Med # sec	41.9	31.1	28.7	27.5	340.7	3.0	4.0
Mean # sec	42.4	32.7	30.5	31.2	464.0	3.3	4.6
Med # Profiles	1,362	931	553	394	2,158	545	283
Med # Obs	302,790	177,573	1,344,974	959,256	–	–	–
Med # CV evals	10	10	7	6	–	–	–
Comp. Complex	$O(Nm)$	$O(Nm)$	$O(N_2m^2)$	$O(N_2m^2)$	$O(\tilde{n}_y^2)$	$O(Nm)$	$O(\tilde{n}_y^2)$

We briefly and roughly compare the computational cost compared to a pointwise approach like [Kuusela and Stein \(2018\)](#). If we focus on temperature and use 10 scores with 40,782 grid points and a radius of 1250 kilometers for the maximum likelihood and prediction, we get similar cross-validated prediction errors (results are not presented here), and the mean time to compute the likelihood maximum over all grid points is approximately 169 seconds. By considering only the steps for temperature, the computations take approximately 3,000 core-hours. The naive comparison is 10 Matérn likelihoods to maximize compared to 58 for 58 separate pressure levels. One must also take into account the extra step of marginal covariance estimation, estimating the nugget variance, and estimating the scores by least squares for each grid point. Since estimating the scores and nugget typically takes less than 5 seconds, we estimate that the time for these extra steps is less than 40 seconds per grid point, which is approximately equivalent to the time it takes to compute the maximum of 3 likelihoods. Thus, our approach can get comparable predictions for each pressure level and the entire pressure dimension in approximately one-fifth to one-fourth (13/58) of the time of a pointwise approach for 58 levels.

A.5. Comparison of Estimated and Working Correlation. For each location, we compute the estimated marginal correlation in pressure

$$\rho(p_1, p_2) = \frac{C(p_1, p_2)}{\sqrt{C(p_1, p_1)C(p_2, p_2)}},$$

where $C(p_1, p_2)$ is our estimated covariance, at points $p_1 = p$ and $p_2 = p + p_{\text{lag}}$ for $p = 0, 50, 100, \dots, 1900, 1950$ for both temperature and salinity and lags $p_{\text{lag}} = 10, 25, 50, 100, 200, 500$. Next, we consider the average and median over locations. The results of this are plotted in Figure 13, with comparison to the working covariance used in the mean estimation. The working covariance provides an adequate approximation of the covariance at each lag and considerably improves compared to no specification of the correlation structure.

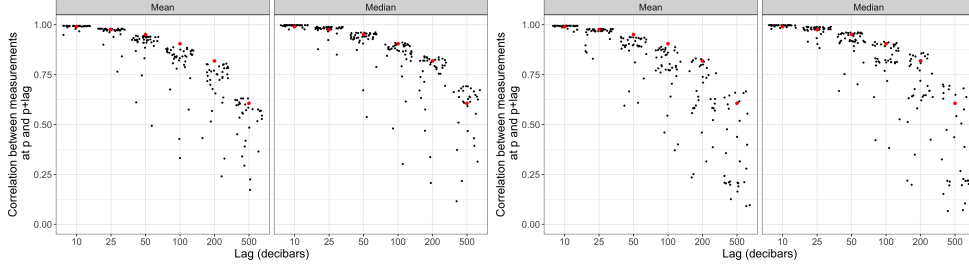


FIG 13. *Estimated correlation versus working correlation used (Left) temperature (Right) salinity for measurements different lags apart. Each black point represents an average over locations for one p_1 and $p_1 + p_{\text{lag}}$. The black dots within the same lag describe the correlation at different p_1 . The points have been randomly jittered horizontally for visualization. The working correlation is in red.*

A.6. Simultaneous Prediction Bands. To develop simultaneous prediction bands, we extend the approach of [Choi and Reimherr \(2018\)](#) to our model. They focus on the statistic

$$W_\theta = \sum_{k=1}^{\infty} \frac{\lambda_k}{c_k^2} \left(\frac{Z_{*,k}}{\sqrt{\lambda_k}} \right)^2$$

for $\lambda_k = \text{Var}\{Z_{*,k}|Y^0\}$ and some chosen constants c_k . In practice, the sum in W_θ must be truncated to a finite number K_1 . Since W_θ can be written as the quadratic form of a random Gaussian vector, the `imhof` function in R is used to compute its quantiles $\{q_\alpha | P(W_\theta > q_\alpha) = \alpha\}$. The band is of the form

$$B = \left\{ h \in \mathbb{W}_2, \left| h(p) - \sum_{k=1}^{\infty} \phi_k(p) \mathbb{E}\{Z_{*,k}|Y\} \right| \leq r(p) + u(p) \right\}$$

where $r(p) = \sqrt{\xi \sum_{k=1}^{\infty} c_k^2 \phi_k(p)^2}$ and ξ is the $1 - \alpha_1$ quantile of W_θ . Here, we have $u(p) = q_{\alpha_2/(2m_i)} \sqrt{\kappa(p)}$ where $\alpha = \alpha_1 + \alpha_2$. Using α_1 and α_2 gives a Bonferroni correction to turn the confidence interval into a prediction interval for the profile i that was left out. Here, $\alpha_1 = \alpha_2 = .02275$, which corresponds to $\alpha = .04550$ or a 95.4% prediction band. We use their choice of $c_k^2 = \sqrt{\text{Var}\{Z_{*,k}|Y^0\}} = \sqrt{\lambda_k}$. Although this creates bands that may not have favorable theoretical coverage properties, as discussed in Section 3 of [Choi and Reimherr \(2018\)](#), in practice they work well for both temperature and salinity.

A.7. Additional R packages used. We note here that our work depends on the R packages [Chang et al. \(2018\)](#); [Wickham \(2016\)](#); [Wickham et al. \(2019\)](#) which we have not mentioned above.

A.8. Comparison of Predictions with Kuusela and Stein (2018). We evaluate our functions at fixed pressure values and compare our predictions (including the mean and conditional prediction) to those of Kuusela and Stein (2018) for 2012. In general, the differences between the predictions are relatively small. Near Antarctica, there are more differences, possibly because of the differences in the mean functions used. At 1500 dbar, there appear to be more differences in the North Atlantic.

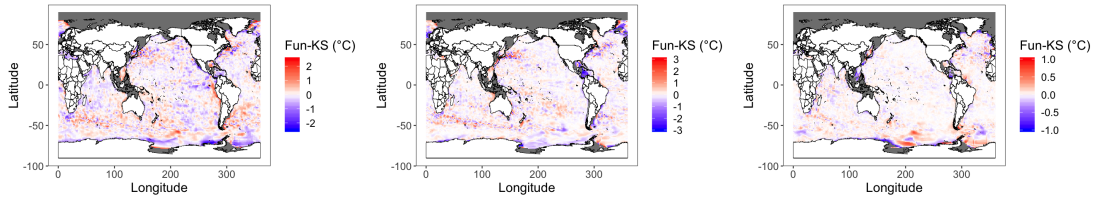


FIG 14. Comparison between functional predictions and Kuusela and Stein at fixed pressure levels for 2012, (Left) 10 dbar, (Middle) 300 dbar, (Right) 1500 dbar.

A.9. Empirical and Model-Based Variance Estimates. We compare the empirical and theoretical variance estimates for the residuals. After breaking pressure into 50 decibar increments, we plot the difference in quantiles for the two variances against the theoretical quantile. In Figure A.9, exact normality would have a horizontal line at 0. There appear to be some differences from normality, especially for salinity. For quantiles near the median, the variance estimates tend to be conservative, with the opposite effect near the extremes. A similar relationship is seen in Kuusela and Stein (2018). The variance estimates at deeper pressures (> 1000 dbar) are generally more conservative than those in the first 500 dbar.

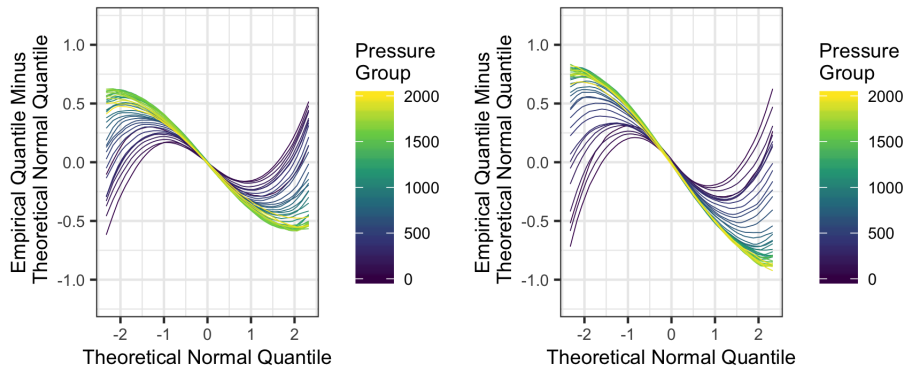


FIG 15. Quantile plots for predicted residuals, grouped by 50 dbar pressure increments (Left) temperature and (Right) salinity.

A.10. General functions of temperature and salinity. Denote the estimated functions of temperature and salinity at a fixed location s_0 and time d_0 as

$$(20) \quad T(p) = \mu_T(p) + \sum_{k=1}^{K_1} Z_k \phi_k(p), \text{ and } S(p) = \mu_S(p) + \sum_{k=1}^{K_2} W_k \psi_k(p)$$

where μ_T and μ_S are the respective mean functions and

$$\begin{pmatrix} Z \\ W \end{pmatrix} \Big| Y^0 \sim N \left(\begin{pmatrix} \theta_1 \\ \theta_2 \end{pmatrix}, \begin{pmatrix} \Sigma_{11} & \Sigma_{12} \\ \Sigma_{21} & \Sigma_{22} \end{pmatrix} \right).$$

We present two general methods for estimating the distribution of some function of $T(p)$ and $S(p)$, which we denote $g(T(p), S(p))$. The first is a conditional simulation or parametric bootstrap approach: simulate $T_b(p)$ and $S_b(p)$ according to their estimated distributions and compute $g(T_b(p), S_b(p))$, repeating this process a large number of times $b = 1, \dots, B$. The average and variability of the bootstrapped values $g(T_b(p), S_b(p))$ give estimates for the distribution of $g(T(p), S(p))$.

The second approach is due to the Delta method, a commonly-used tool used in statistics. Suppose that $g(T(p), S(p))$ has continuous first partial derivatives

$$\nabla g(p) = \left(\frac{\partial g(T(p), S(p))}{\partial t}, \frac{\partial g(T(p), S(p))}{\partial s} \right)^\top$$

at $\mathbb{E}\{T(p)|Y^0\} = \mu_T(p) + \phi(p)^\top \theta_1$ and $\mathbb{E}\{S(p)|Y^0\} = \mu_S(p) + \psi(p)^\top \theta_2$. By the multivariate Delta method, $g(T(p), S(p))$ converges to a normal distributed random variable in distribution with mean

$$\mu_g(p) = g(\mathbb{E}\{T(p)|Y^0\}, \mathbb{E}\{S(p)|Y^0\})$$

as the matrix $\begin{pmatrix} \Sigma_{11} & \Sigma_{12} \\ \Sigma_{21} & \Sigma_{22} \end{pmatrix}$ decreases to the 0 matrix. Furthermore, letting

$$C(p_1, p_2) = \begin{pmatrix} \phi(p_1)^\top & 0 \\ 0 & \psi(p_1)^\top \end{pmatrix} \begin{pmatrix} \Sigma_{11} & \Sigma_{12} \\ \Sigma_{21} & \Sigma_{22} \end{pmatrix} \begin{pmatrix} \phi(p_2) & 0 \\ 0 & \psi(p_2) \end{pmatrix} \in \mathbb{R}^{2 \times 2},$$

the limiting variance of $g(T(p), S(p))$ is $\Sigma_g(p) \approx \nabla g(p)^\top C(p, p) \nabla g(p)$. This gives a natural way to estimate differentiable functions of temperature and salinity using a linear approximation to the function g .

A.11. Integrals and Derivatives. Here, we demonstrate how, for a fixed location, the distributions of integrals and derivatives can be estimated naturally from our estimates. Using the notation for temperature, for any $p^* \in (0, 2000]$, the integral $I_{p^*} = \int_0^{p^*} T(p) dp$ is normally distributed with mean and variance

$$\begin{aligned} \mathbb{E} \left(I_{p^*} \Big| Y^0 \right) &= \int_0^{p^*} \mathbb{E}(T(p)|Y^0) dp = \int_0^{p^*} \mu_T(p) dp + \int_0^{p^*} \phi(p)^\top dp \theta_1 \\ \text{Var} \left(I_{p^*} \Big| Y^0 \right) &= \left(\int_0^{p^*} \phi(p)^\top dp \right) \Sigma_{11} \left(\int_0^{p^*} \phi(q) dq \right) \end{aligned}$$

by exchanging the order of integration and using (12), interpreting $\int_0^{p^*} \phi(p)^\top dp$ as the integral applied element-wise to $\phi(p)^\top$. The ℓ th derivative of the prediction is also normally distributed, with mean and variance

$$\mathbb{E}\left(T^{(\ell)}(p)\middle|Y^0\right) = \mu_T^{(\ell)}(p) + \phi^{(\ell)}(p)^\top \theta_1, \text{ and } \text{Var}\left(T^{(\ell)}(p)\middle|Y^0\right) = \phi^{(\ell)}(p)^\top \Sigma_{11} \phi^{(\ell)}(p)$$

for $\ell = 1, 2$. The integral $\int_0^{p^*} \phi_k(p) dp$ for each p^* and k and the derivatives $\mu_T^{(\ell)}$ and $\phi_k^{(\ell)}(p)$ can be computed quickly using the `inprod` and `eval.basis` functions, respectively, in the `fda` package in R (Ramsay et al., 2018). The integrals are easily extended to arbitrary bounds within $[0, 2000]$.

A.12. Delta Method for Ocean Heat Content. The Delta method estimate of the conditional mean of Q is

$$\mathbb{E}\{Q|Y^0\} = c_p \rho \int_0^{p^*} \Theta(\mathbb{E}\{T(p)|Y^0\}, \mathbb{E}\{S(p)|Y^0\}, p) dp.$$

Also, following the steps and using the definitions in Subsection A.10,

$$\text{Var}\{Q|Y^0\} \approx c_p^2 \rho^2 \int_0^{p^*} \int_0^{p^*} \nabla\Theta(p_1)^\top C(p_1, p_2) \nabla\Theta(p_2) dp_1 dp_2$$

where $\nabla\Theta(p)$ are the derivatives of Θ with respect to temperature and salinity at pressure p . The closed form expressions of the partial derivatives of Θ with respect to temperature and absolute salinity are available through TEOS-10 (McDougall and Barker, 2011). We use these as the expression for $\nabla\Theta(p)$, suggesting that the derivative for absolute salinity approximates the derivative for practical salinity well on the interval 0 to 2000 dbar. Since these are very similar quantities and the salinity plays a small role in conservative temperature compared to temperature, this approximation is justified. Since conservative temperature is a nonlinear function of temperature and salinity, exact expressions for these integrals are not available, but the integral can be approximated on an arbitrarily fine grid of pressure.

D. YARGER
S. STOEV
T. HSING
DEPARTMENT OF STATISTICS
UNIVERSITY OF MICHIGAN
ANN ARBOR, MICHIGAN 48109 USA
E-MAIL: dyarger@umich.edu
sstoev@umich.edu
thsing@umich.edu